



The connection between Labrador Sea buoyancy loss, deep western boundary current strength, and Gulf Stream path in an ocean circulation model

Stephen G. Yeager*, Markus Jochum

National Center for Atmospheric Research, Boulder, CO, USA

ARTICLE INFO

Article history:

Received 30 October 2008

Received in revised form 24 June 2009

Accepted 29 June 2009

Available online 10 July 2009

Keywords:

Gulf Stream

Deep western boundary current

Mixed thermohaline boundary conditions

Water mass transformation

North Atlantic

ABSTRACT

The sensitivity of the North Atlantic gyre circulation to high latitude buoyancy forcing is explored in a global, non-eddy resolving ocean general circulation model. Increased buoyancy forcing strengthens the deep western boundary current, the northern recirculation gyre, and the North Atlantic Current, which leads to a more realistic Gulf Stream path. High latitude density fluxes and surface water mass transformation are strongly dependent on the choice of sea ice and salinity restoring boundary conditions. Coupling the ocean model to a prognostic sea ice model results in much greater buoyancy loss in the Labrador Sea compared to simulations in which the ocean is forced by prescribed sea ice boundary conditions. A comparison of bulk flux forced hindcast simulations which differ only in their sea ice and salinity restoring forcings reveals the effects of a mixed thermohaline boundary condition transport feedback whereby small, positive temperature and salinity anomalies in subpolar regions are amplified when the gyre spins up as a result of increased buoyancy loss and convection. The primary buoyancy flux effects of the sea ice which cause the simulations to diverge are ice melt, which is less physical in the diagnostic sea ice model, and insulation of the ocean, which is less physical with the prognostic sea ice model. Increased salinity restoring ensures a more realistic net winter buoyancy loss in the Labrador Sea, but it is found that improvements in the Gulf Stream simulation can only be achieved with the excessive buoyancy loss associated with weak salinity restoring.

© 2009 Elsevier Ltd. All rights reserved.

1. Introduction

Simulations of the North Atlantic in non-eddy resolving ocean general circulation models (OGCMs) have historically suffered from poor representation of the strength and path of the Gulf Stream (Dengg et al., 1996). The resulting large biases in the high-latitude temperature and salinity fields seriously undermine the utility of these models for investigating oceanic and coupled climate processes in the North Atlantic. For instance, negative sea surface temperature (SST) biases east of the Grand Banks exceed 9 °C in one widely used coupled climate model (Large and Danabasoglu, 2006).

Numerous studies have demonstrated that a marked improvement in the realism of the modeled North Atlantic circulation is obtainable at so-called eddy-resolving resolutions (horizontal resolution 0.1°) in which the first mode baroclinic Rossby radius is resolved and the mesoscale energy spectrum approaches observed levels (e.g., Bryan et al., 2007; Smith et al., 2000; Hurlburt and Hogan, 2000; Oschlies, 2002; Brachet et al., 2004). However, the com-

putational expense of such high horizontal resolution precludes the use of eddy-resolving models for long simulations or as the ocean component in coupled climate models.

A remedy for the Gulf Stream (GS) problem for non-eddy resolving (coarse) resolutions has been elusive, but important sensitivities have been identified. A stronger deep western boundary current (DWBC) pushes the latitude of the GS separation point to the south (Tansley and Marshall, 2000; Thompson and Schmitz, 1989; Ezer and Mellor, 1992; Dai et al., 2005). The DWBC is coupled to the GS through entrainment of upper DWBC water under the GS at the crossover point (Spall, 1996), and bottom-vortex stretching induced by a strong downslope DWBC south of the Grand Banks enhances the strengths of the northern recirculation gyre (NRG) and the North Atlantic Current (NAC) (Zhang and Vallis, 2007, hereafter referred to as ZV07). Since the DWBC is related to the strength of deep convection and thermohaline forcing at high latitudes, perturbing the surface density in deep-water formation regions can have pronounced effects on GS circulation (Gerdes and Koberle, 1995).

Coarse resolution OGCMs are by necessity too viscous, because they must satisfy numerical constraints associated with the large grid spacing (Large et al., 2001). However, a significantly improved Labrador current and sea ice distribution can be obtained by lowering horizontal viscosity at the expense of increased grid-scale noise

* Corresponding author. Address: Climate and Global Dynamics Division, National Center for Atmospheric Research, Boulder, CO 80307-3000, USA. Tel.: +1 303 497 17 21.

E-mail address: yeager@ucar.edu (S.G. Yeager).

(Jochum et al., 2008). Less momentum diffusion has been linked to a strengthening of the subpolar and northern recirculation gyres, and improved GS separation in 1° OGCMs (ZV07; Doney et al., 2003).

Several studies have demonstrated that the GS system is sensitive to the details of how sub-gridscale mixing is parameterized. Danabasoglu et al. (2008) find that deep convection in the Labrador, Greenland, Irminger, and Norwegian Seas is considerably enhanced with a parameterization for near surface mesoscale eddy fluxes (Ferrari et al., 2008). Allowing spatial and temporal variations in the thickness diffusivity (Gent and McWilliams, 1990) generates deeper Labrador Sea convection and reduces the negative temperature biases east of the Grand Banks (Eden et al., 2009). When physically-based latitudinal structure is added to the background vertical diffusivity such that diapycnal mixing is enhanced in the subtropics, deep convection is more robust, the DWBC strengthens, and the GS shifts southward (Jochum, 2008).

The origins of systematic errors in OGCMs are generally explored in uncoupled configurations in which the ocean surface boundary conditions are strongly constrained by observations. While this approach can generate quite realistic ocean simulations in the Tropics, the North Atlantic is a particularly challenging region to model because of the importance of sea-ice thermodynamics, buoyancy flux and bottom pressure torque. In the present work, we investigate the sensitivity of the North Atlantic circulation in a coarse resolution OGCM to surface forcing. We focus on the model response to different forcing choices which are commonplace in ocean model development, an activity which places a premium on the realism of the ocean boundary conditions. The effects of the following are compared in configurations which use prescribed atmospheric forcing: (1) use of a prognostic versus a diagnostic sea ice model, (2) the use of interannual versus repeating annual atmospheric conditions, and (3) the strength of surface salinity restoring. Configurations which maximize DWBC transport show dramatic and unprecedented improvement in NAC strength and GS path for the 1° version of the ocean component of CCSM; however, this is achieved only when the surface water mass formation of Atlantic deep water exceeds reasonable rates. Excessive sur-

face transformation is shown to be an artifact of the circulation feedbacks arising from mixed thermohaline boundary conditions.

2. Description of the model and experiments

The ocean and sea ice models used for all experiments are development versions of the component models of the Community Climate System Model (CCSM). The suite of models corresponds to CCSM 3.5, which is an interim version preceding the future release of CCSM 4. The ocean model is a z-coordinate, primitive equation global ocean model based on the Parallel Ocean Program (POP) developed at the Los Alamos National Laboratory (Smith et al., 1992; Dukowicz and Smith, 1994). The curvilinear horizontal mesh is nominally 1° with 320 zonal and 384 meridional grid points and has its northern grid pole displaced into Greenland. The ocean model differs from the CCSM 3 version described at length in Danabasoglu et al. (2006) as follows:

- The vertical grid resolution is increased from 40 to 60 levels with a layer of constant cell thickness of 10 m extending to 160 m depth.
- The Ferrari et al. (2008) near-surface eddy flux parameterization is implemented (Danabasoglu et al., 2008) with stratification-dependent enhancement of the isopycnal thickness diffusivity (Danabasoglu and Marshall, 2007).
- The anisotropic horizontal viscosity is reduced by one to two orders of magnitude (Jochum et al., 2008).
- A parameterization for tidally-driven vertical diffusivity is implemented (Jayne, 2009).

The North Atlantic bathymetry of the model shown in Fig. 1 highlights some of the geographic features salient to the simulation of the Atlantic circulation and gives a sense of the enhanced resolution in the vicinity of Greenland associated with the converging meridional lines of the 1° POP grid.

In each experiment (see Table 1), surface fluxes are computed from bulk formulae using the prognostic ocean model SST and an

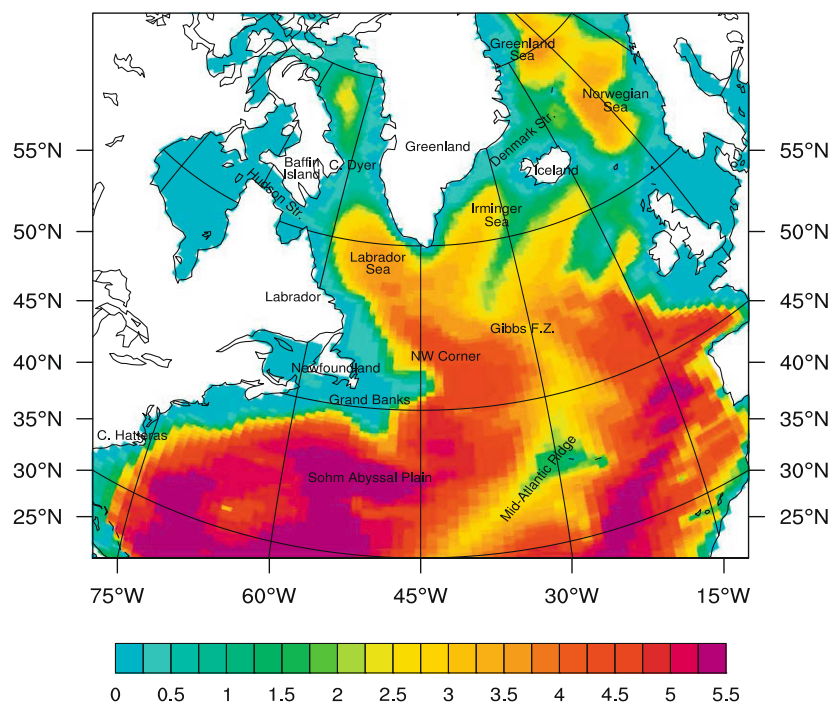


Fig. 1. Ocean bathymetry (km) from the POP 1° model with geographical features mentioned in the text.

observed atmospheric state using the methods described in Large et al. (1997). The prescribed atmosphere is a combination of 6-hourly atmospheric state data from NCEP reanalysis (Kalnay et al., 1996), daily radiation from the International Satellite Cloud Climatology Project (ISCCP-FD; Zhang et al., 2004), monthly precipitation from Xie and Arkin (1996) and the Global Precipitation Climatology Project (GPCP; Huffman et al., 1997), and climatological river runoff. The raw data have been adjusted to ameliorate known systematic biases. All experiments except one use the interannually-varying forcing dataset (CORE.2-IAF) of Large and Yeager (2008), spanning 1949–2006. Experiment B2 uses a repeating normal year forcing (CORE.2-NYF), which is identical to CORE.1-NYF of Large and Yeager (2004) but uses updated adjustment factors. The initial condition for the ocean in all experiments is a state of rest, with temperature and salinity prescribed from the global climatological distribution of the 1998 World Ocean Atlas (Levitus et al., 1998) merged with the Polar Science Center Hydrographic Climatology (Steele et al., 2001); this combined dataset is hereafter referred to as WOA/PHC.

In ocean only experiments (cases A and A1), a diagnostic sea ice model prescribes daily observed sea ice fraction from satellite measurements (Comiso, 1999), and also computes under-ice heat and freshwater fluxes (see Appendix A). The ice fraction observations are available from 1979 onwards, and a climatological year of daily ice fraction is used for prior years in hindcast experiments. Note that this diagnostic sea ice model is an infinite source of heat and freshwater, because the sea ice concentration is prescribed. The data ice model is replaced by a dynamic and thermodynamic sea ice model in coupled ocean–ice experiments (cases B, B1, and B2). Its details are documented in Holland et al. (2006), and its impact on the thermohaline forcing is discussed in detail in the following sections.

3. Mean results

The barotropic streamfunction in case A separates from the North American coast close to Cape Hatteras (Fig. 2a). This result is an improvement over similarly-configured CCSM 3 POP solutions, in which the anticyclonic subtropical gyre extended to Newfoundland, and is primarily attributable to the recent inclusion of lower horizontal viscosity and parameterized near-surface eddy fluxes in the model. The viscosity changes increase the strength of the Labrador Gyre and generate stronger, narrower coastal currents (Jochum et al., 2008), while improved representation of near-boundary eddy mixing results in deeper convection in the Labrador Sea (Danabasoglu et al., 2008). As a result, the DWBC is deeper and stronger than in CCSM 3, and the GS separation latitude is more realistic.

However, significant and longstanding biases in the North Atlantic circulation remain evident. Observational estimates suggest that the northern recirculation gyre (NRG), the cyclonic gyre south of the Grand Banks, should be as strong as 20 Sv (Hogg et al., 1986), but this circulation is minimal in case A. The Gulf Stream extension is much too zonal, and the lack of a strong North Atlantic Current (NAC, defined here as the northward extension of

the GS past the Grand Banks) is reflected in the weak streamfunction gradient east of the Grand Banks. By contrast, in high resolution models which do well at simulating the NAC (Smith et al., 2000), the boundary between the subtropical and subpolar gyres is characterized by sharp gradients of depth-integrated flow and the positive barotropic streamfunction penetrates well north of 45°N. Coupling to a fully active atmosphere model exacerbates the overly zonal and diffuse GS problem (see for example Large and Danabasoglu, 2006, their Fig. 3), but an improved circulation is obtained when the data ice model used in case A is replaced with an active sea ice model, as in case B (Fig. 2b). The NRG is stronger in this configuration, although still anemic at only 10 Sv. The sharper barotropic streamfunction gradients reflect more jet-like Gulf Stream and NAC flow, and the recirculation cells east of the Grand Banks indicate more vigorous meridional currents along the shelf.

The circulation in B remains distinctly different from that obtained in A throughout the 58 year cycle of forcing. The 5-year mean streamfunctions from the two experiments corresponding to 2002–2006 are shown in panels c and d of Fig. 2. The NRG in B exceeds 15 Sv in this time period, and the gradients in barotropic flow show even greater resemblance to streamfunctions computed from eddy-resolving models. There is a positive trend in the strength of the NRG in both solutions which may be partially explained by the increasing NAO index over the hindcast years (Joyce et al., 2000; Biastoch et al., 2008), but an unrealistic feedback associated with the mixed thermohaline boundary conditions contributes to the trend. The interannual variability in the North Atlantic circulation is examined closely in the next section.

The poor representation of the NAC leads to large temperature and salinity biases in the mid- to high-latitude North Atlantic. The WOA/PHC climatology clearly shows the sharp northward excursion of isotherms east of the Grand Banks (50°W, 40°N) associated with the NAC, which transports warm and salty subtropical water into the Northwest Corner region (Rossby, 1996) where it retroflects to the east (Fig. 3). Because of an overly zonal GS, the temperature east of the Grand Banks at 175 m depth is more than 9 °C too cold in case A (Fig. 3c and d), while the salinity field is too fresh by about 0.8 psu. This cold/fresh bias extends to below 500 m, but has its maximum at about 200 m, and its surface signature in coupled configurations results in significant perturbation of the North Atlantic atmosphere. A more vigorous NAC in experiment B (Fig. 3e and f) roughly halves both the spatial extent and magnitude of model biases east of the Grand Banks. Zonal gradients of temperature and salinity offshore of the Grand Banks are much improved in B, but the penetration of large gradients into the Northwest Corner region is lost in both simulations. The weak NAC is compensated by overly strong northward flow on the eastern side of the basin, especially in A. This results in a steady advection of excessively warm, salty upper ocean water in a crescent extending from Europe to Greenland and into the Labrador Sea.

The stronger NRG and improved NAC path in case B are related to much stronger, denser DWBC flow which is in better agreement with observed estimates of the meridional transports on the continental shelf east of Grand Banks. Fig. 4 shows grid-oriented meridional velocity profiles from experiments A and B as a function of depth along a model grid line of nearly constant latitude at 43°N,

Table 1
Description of experiments.

Experiment	Configuration	Forcing	Control case	Perturbation
A	Ocean only	CORE 1949–2006	–	–
A1	Ocean only	CORE 1949–2006	A	$Q_{min} = 0 \text{ W/m}^2$
B	Ocean–ice	CORE 1949–2006	–	–
B1	Ocean–ice	CORE 1949–2006	B	Strong salinity restoring ($V_p = 50 \text{ m/30 days}$)
B2	Ocean–ice	CORE NYF	B	Repeat annual forcing

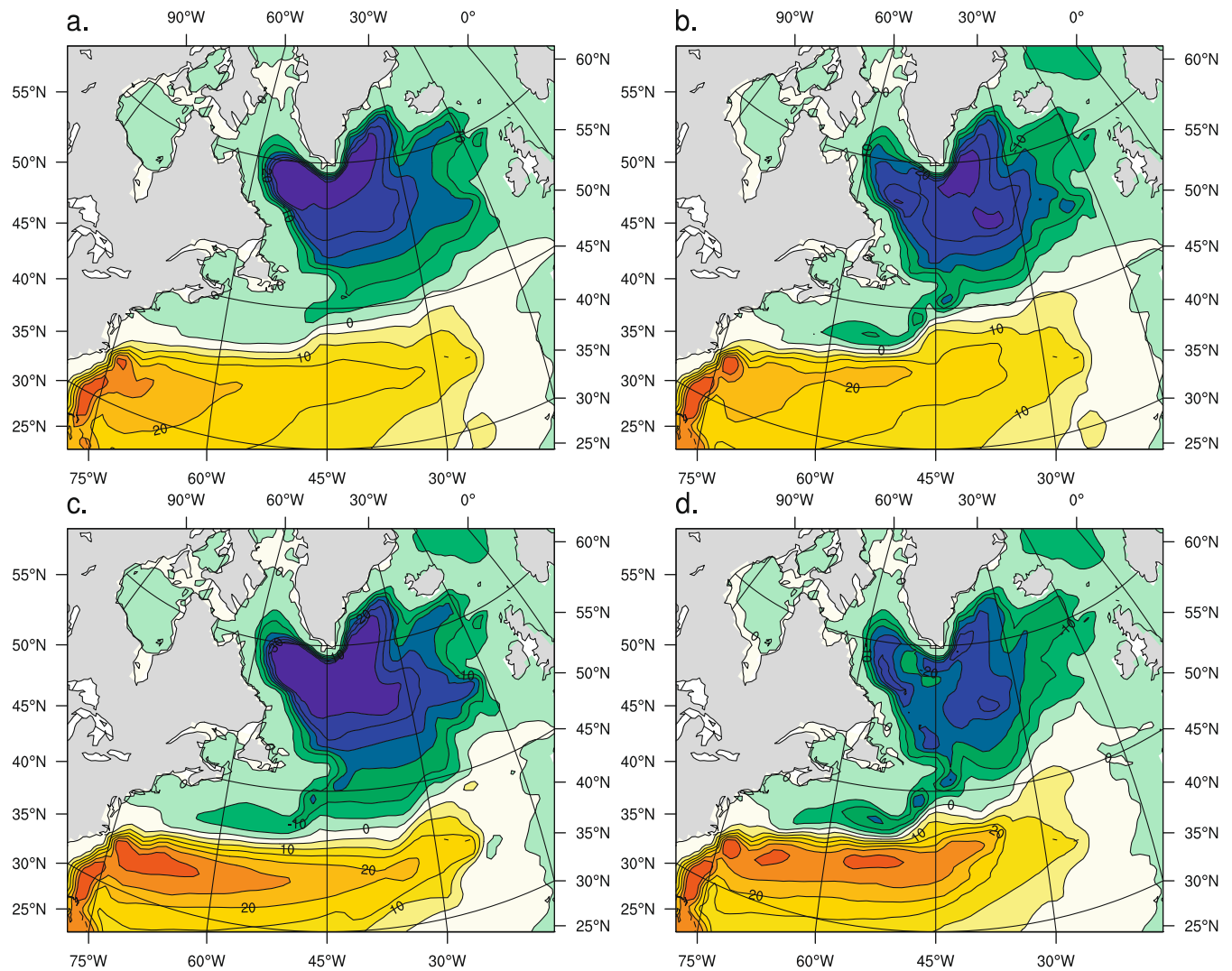


Fig. 2. Mean barotropic streamfunction (Sv) from (a and c) experiment A and (b and d) experiment B. The top panels (a and b) correspond to simulation years 16–20 (forcing years 1964–1968) and the bottom panels (c and d) to simulation years 54–58 (forcing years 2002–2006). The contour interval is 5 Sv.

for both time periods plotted in Fig. 2. The location was chosen to facilitate comparison with observed current profiles from moored arrays and ship transects taken between 1999 and 2005 along the western end of the WOCE A2 line (Schott et al., 2004, hereafter referred to as S04; Schott et al., 2006, hereafter referred to as S06, see their Fig. 1). For comparison with these observations, we plot the isopycnals $\sigma_0 = 27.68, 27.74, 27.80,$ and 27.88 kg/m^3 which demarcate the upper bounds of the observed water masses: Upper Labrador Sea Water, Labrador Sea Water, Gibbs Fracture Zone Water, and Denmark Strait Overflow Water. The DWBC in A is extremely weak in the first half of the simulation, with maximum velocity less than 4 cm/s, and no significant transport below 1000 m (Fig. 4a). The active ice model in B results in a much denser and more vigorous DWBC by year 20 (Fig. 4b) with the bulk of the southward flow below 1000 m, which is more in line with observations. Both simulations show a rise in DWBC transport with time (Fig. 4c and d), but with consistently larger and denser flow in case B. S06 report a mean southward transport along the shelf of $17.5 \pm 6.8 \text{ Sv}$ for water denser than $\sigma_0 = 27.68 \text{ kg/m}^3$. The transports for experiments A and B are 4.1 and 14.8 Sv, respectively, for simulation years 16–20, and 11.4 and 17.4 Sv for years 54–58. The total transport is more realistic in B, but the DWBC water in B is in general too dense, while transport in the highest density range ($\sigma_0 > 27.88 \text{ kg/m}^3$) is missing (see Section 6.2 for discus-

sion). The NAC is weak in A, and although it is considerably strengthened in B, the simulated northward flow is still much lower than observed. The current speed in the offshore jet in B is about 16 cm/s near the surface and extends to below 1000 m, but measurements from S06 indicate NAC velocity in excess of 60 cm/s at this latitude.

The horizontal velocity field in the vicinity of Grand Banks is shown at a depth of 2400 m in Fig. 5 for the final 5 years of each of the hindcast experiments. At this stage in the simulation, the boundary current in case A penetrates around the southern tip of the Grand Banks shelf and forms a southward flowing jet along the coast of North America which enhances the strength of the NRG (Fig. 2c). The abyssal flow in case B is nearly uniformly stronger throughout the region. Both experiments (Fig. 5a and b) exhibit two distinct branches of southwest flow, in line with the estimates of DWBC pathways from Schmitz and McCartney (1993): one along the continental slope and the other traversing the Sohm Abyssal Plain.

A correlation between the strengths of the DWBC and the NAC has been observed (S04), and ZV07 have argued that the bottom vortex stretching induced by the downslope DWBC east of the Grand Banks contributes to the strength of the northward offshore NAC. This explanation is supported by the fact that the average bottom vertical velocity, W_B , is five times larger in experiment B

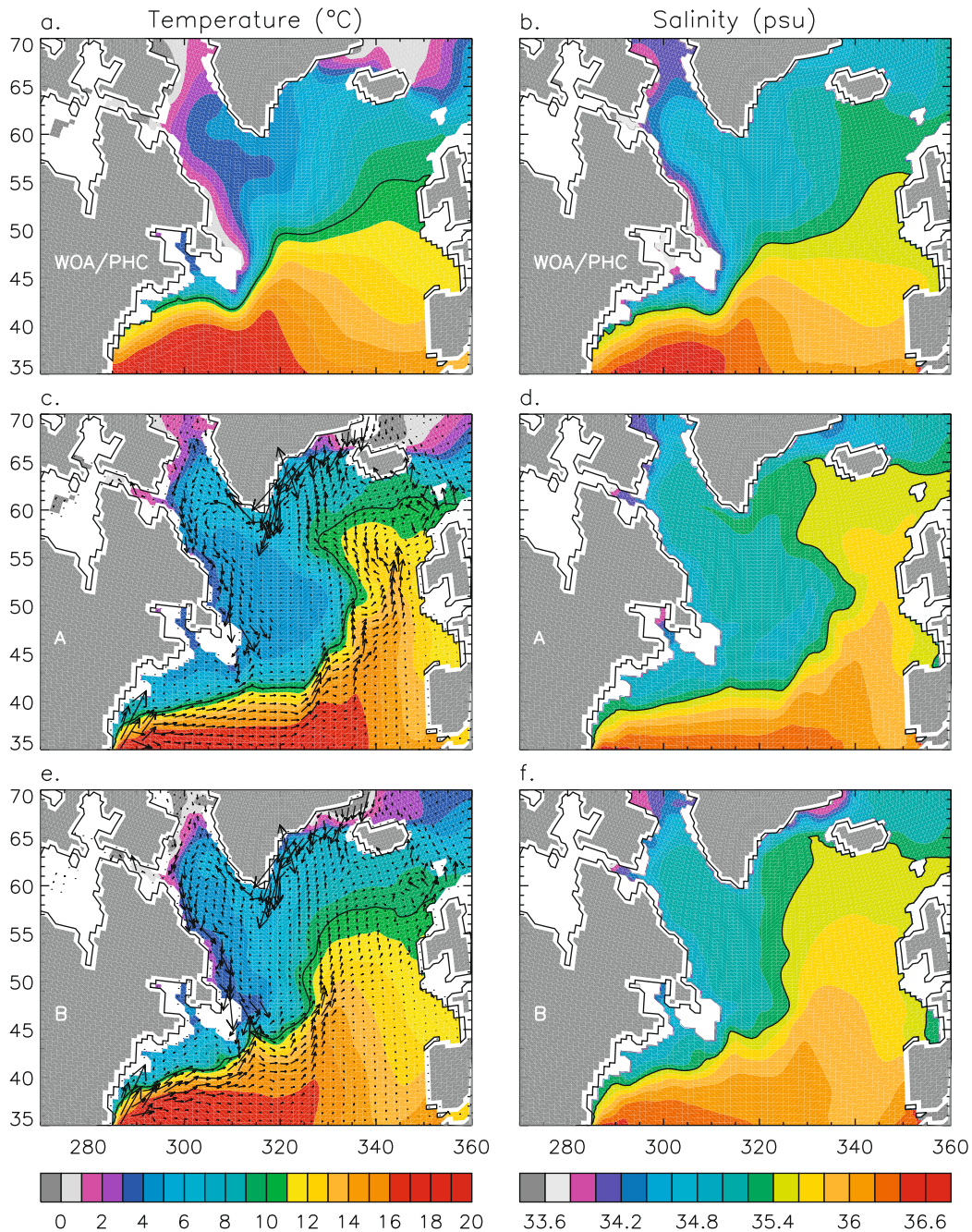


Fig. 3. Temperature (left panels) and salinity (right panels) at 175 m depth from (a and b) WOA/PHC climatology and from model years 54–58 (forcing years 2002–2006) of (c and d) experiment A and (e and f) experiment B. Contour lines are drawn for 10 °C and 35.4 psu. The velocity field at this depth is overlaid on the temperature plots for A and B.

than in A in a region east of the Grand Banks ($W_B = -5.2 \times 10^{-5}$ m/s compared to -0.9×10^{-5} m/s averaged over 50–47°W, 44–46°N for simulation years 16–20). ZV07 show that a similar increase in downwelling bottom velocity is needed to achieve a strong cyclonic NRG in their model.

4. Thermohaline forcing feedbacks and gyre spinup

An overview of the inherent problems and necessary compromises associated with forcing ocean and coupled ocean–ice models is provided in Griffies et al. (2009). Applying turbulent surface fluxes using bulk formulae and the evolving model SST is desirable because it mimics the approach used in fully coupled climate mod-

els, it ensures a correct correspondence between the evaporation and the latent heat fluxes, and it provides an effective restoring of ocean SST to observed atmospheric conditions which tends to damp model error. The surface freshwater fluxes are not functions of SSS, and so the prescription of observed freshwater fluxes provides no equivalent damping of sea surface salinity anomalies. Given the large uncertainties in precipitation products (Large and Yeager, 2008), the precipitation flux is likely to be a non-trivial source of error in forced experiments. Therefore, some degree of salinity restoring is generally applied. In experiments A and B, surface salinity is weakly restored globally to the WOA/PHC monthly climatology with a piston velocity, V_p , of 50 m/4 years, with the global mean restoring flux removed so that restoring does not

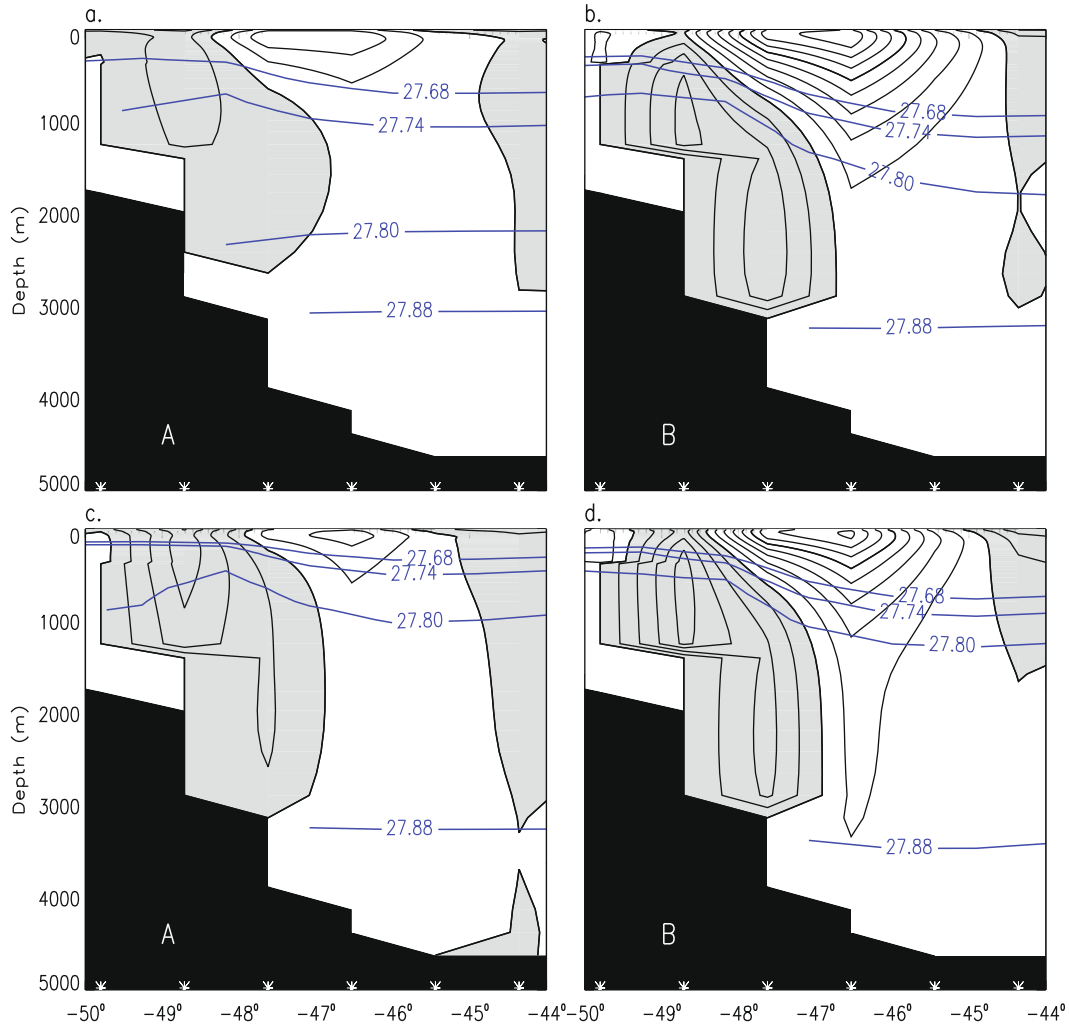


Fig. 4. Meridional velocity sections at $\approx 43.1^\circ\text{N}$ from (a and c) experiment A and (b and d) experiment B, contoured at 2 cm/s. The top panels (a and b) are from simulation years 16–20 (forcing years 1964–1968) and the bottom panels (c and d) are from simulation years 54–58 (forcing years 2002–2006). Shaded regions indicate southward flow. Density is indicated by overlay of σ_0 contours (kg/m^3). The grid resolution is indicated by the asterisks, which show the longitudes of velocity points along the section.

contribute to a drift in mean ocean salinity (see details of NCAR-POP simulation in Griffies et al., 2009).

Boundary conditions which impose strong restoring in temperature but zero or weak restoring in salinity (so called mixed thermohaline boundary conditions) can lead to solutions which are overly sensitive to salinity perturbations in high latitudes (Weaver and Sarachik, 1991; Rahmstorf and Willebrand, 1995; Lohmann et al., 1996; Greatbatch and Peterson, 1996; Griffies et al., 2009). Such forcing eliminates realistic ocean heat transport feedbacks, and as a result, salinity anomalies have an exaggerated effect on the high latitude density field. Spicy (warm/salty) anomalies which advect into the subpolar gyre from the South are strongly restored in temperature (cooled) but not in salinity. The anomalous density flux can give rise to a positive transport feedback if model advection errors lead to overly spicy water in deep-water formation regions. This is because buoyancy is removed very efficiently by cooling, which leads to enhanced convection. The subpolar gyre then spins up, and the anomalous poleward transport of heat and salt is strengthened further (see schematic in Griffies et al., 2009, their Fig. 1). Conversely, a polar halocline catastrophe can result when fresh/cold anomalies in the subpolar gyre lead to increasingly buoyant surface conditions in the North Atlantic which inhibit convection (Zhang et al., 1993).

Positive biases of temperature, salinity, and density develop in the subpolar gyre within 5 years of startup in both experiments A and B. The initial error growth in the North Atlantic deep-water formation regions appears attributable to the spurious drift in the NAC path, but the spinup of the meridional overturning circulation (MOC) through the positive transport feedback described above plays an important role in the subsequent development of high latitude bias in these experiments. The surface biases from late in the simulation (years 54–58 corresponding to forcing years 2002–2006) are shown in Fig. 6. By this time, both solutions exhibit large positive surface biases throughout much of the Labrador, Irminger, North Atlantic, and Norwegian Seas. Negative SST and SSS errors east of the Grand Banks are much reduced in case B, but are replaced by larger positive biases in the Labrador Sea and along the Labrador coast, where the density bias reflects the salinity bias. The bias patterns show the different NAC paths in the two solutions (Fig. 3), with larger surface errors east of mid-Atlantic ridge in case A. The February ice edge in case A is realistic because the observed climatological ice fraction is prescribed by the data ice model, but in case B, the winter ice edge retreats to the vicinity of Hudson Strait.

Differences in the two solutions are attributable to: (1) differences in the exchange of heat and freshwater between the ocean

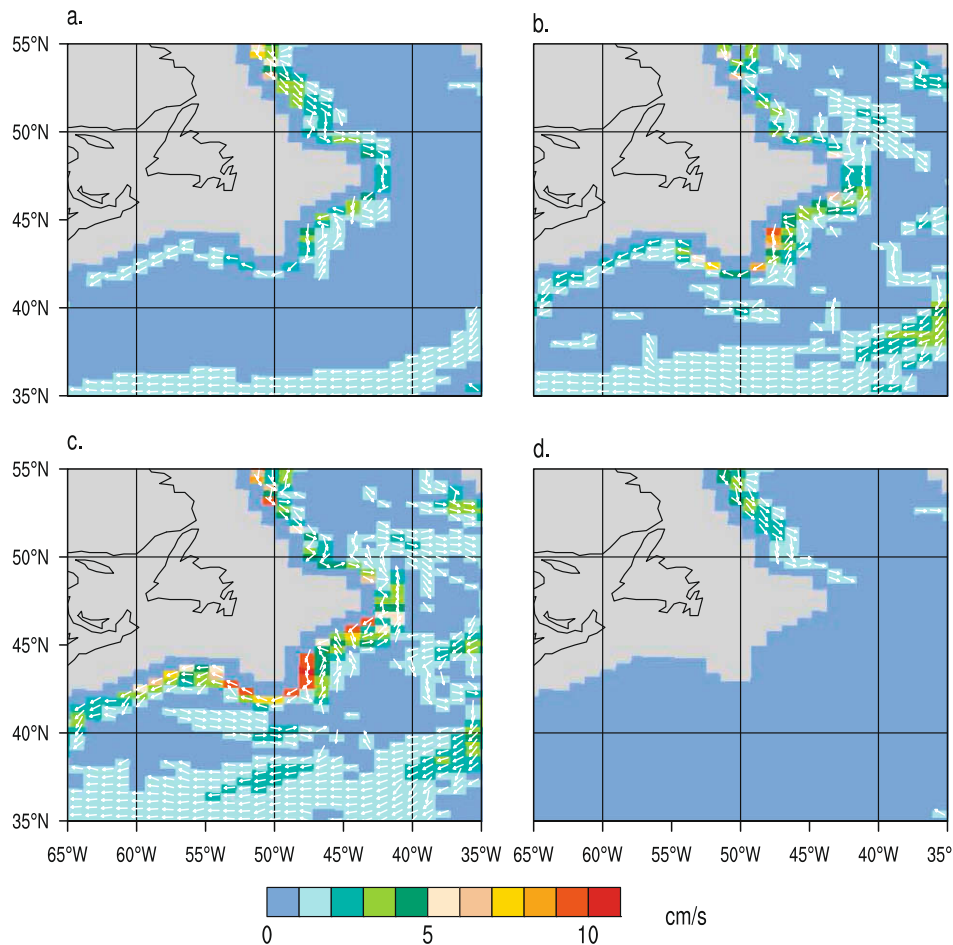


Fig. 5. Horizontal velocity at 2400 m from simulation years 54–58 (forcing years 2002–2006) of experiment (a) A, (b) B, (c) A1, and (d) B1. Arrows give the direction while the color fill gives the magnitude. Arrows are drawn only for speeds greater than 1 cm/s.

and sea ice; (2) differences in air–sea fluxes in the vicinity of the ice edge given that the sea ice extent in B is not coincident with the observed sea ice extent used in A; and (3) differences in forcing arising from the fact that the ocean surface states evolve differently in the two experiments. High latitude forcing is more physical in B compared to A due to (1), because the energy and freshwater budgets of the coupled ocean–ice system will be conservative and the fluxes less ad hoc. However, since the sea ice distribution can evolve in B, (2) will detract from the realism of polar forcing in case B. Since the experiments are initialized identically in T/S and both with a realistic sea ice extent, the initial divergence of the solutions is explained by (1) and (2), and (3) becomes a significant factor after sufficient time has elapsed.

When warm water impinges on the prescribed sea ice in A, the data ice model prescribes negative/positive melt fluxes of heat/freshwater which tend to reduce positive upper ocean biases in A. Since the ice extent remains fixed, the diagnostic melt flux is, in effect, a significant restoring flux for both temperature and salinity. Melt fluxes along the Labrador coast in wintertime in case A routinely exceed 2×10^{-4} kg/m²/s and -60 W/m², a melt rate which implies the loss of more than 0.5 m of ice per winter month. In B, the advection of overly warm water into the Labrador Sea effects a retreat of the sea ice edge, with much less restorative flux. When the ice melt fluxes are turned off in the diagnostic sea ice model (experiment A1), the North Atlantic surface biases develop faster and grow larger than those in the ocean–ice hindcast solution (not shown). Large, positive salinity and density anomalies in A1 result in the strongest DWBC flow of any experiment (Fig. 5c).

Another reason the Labrador Sea quickly gets saltier in simulation B is that there is significantly more brine rejection due to sea ice formation in fall and winter in Baffin Bay and the northern Labrador Sea when running an active sea ice model. The southern advance of the sea ice edge in the cold season in case B necessarily entails ice formation and upper ocean salinification. This is not the case when sea ice concentration is prescribed from observations, because the seawater need not freeze in order for the ice extent to grow and insulate the ocean from the overlying cold air.

In both A and B, the eastward shift of the NAC from its proper longitude just offshore of the Grand Banks to the eastern North Atlantic, and the associated loss of the Northwest Corner retroflection, initiates a feedback-amplified anomalous northward transport of warm, salty water into the subpolar gyre. The error growth is larger in B than in A, because there is less effective restoring and the retreat of the ice edge greatly enhances winter buoyancy loss and MOC strength. It may be that the high latitude surface bias would be comparably large and positive even with a realistic NAC path, if the MOC were too robust, but we have no such simulation to examine. High resolution simulations of the North Atlantic show evidence of Labrador Sea salinization even when the NAC path is much more realistic (Treguier et al., 2005). Nonetheless, we suspect that the large biases in deep-water formation regions in simulations examined herein are strongly tied to GS path error since net meridional transports are reasonable, while the longitudinal distributions of heat/salt transport are not.

The model velocity field is initially set by geostrophic currents induced by the WOA/PHC temperature and salinity distributions.

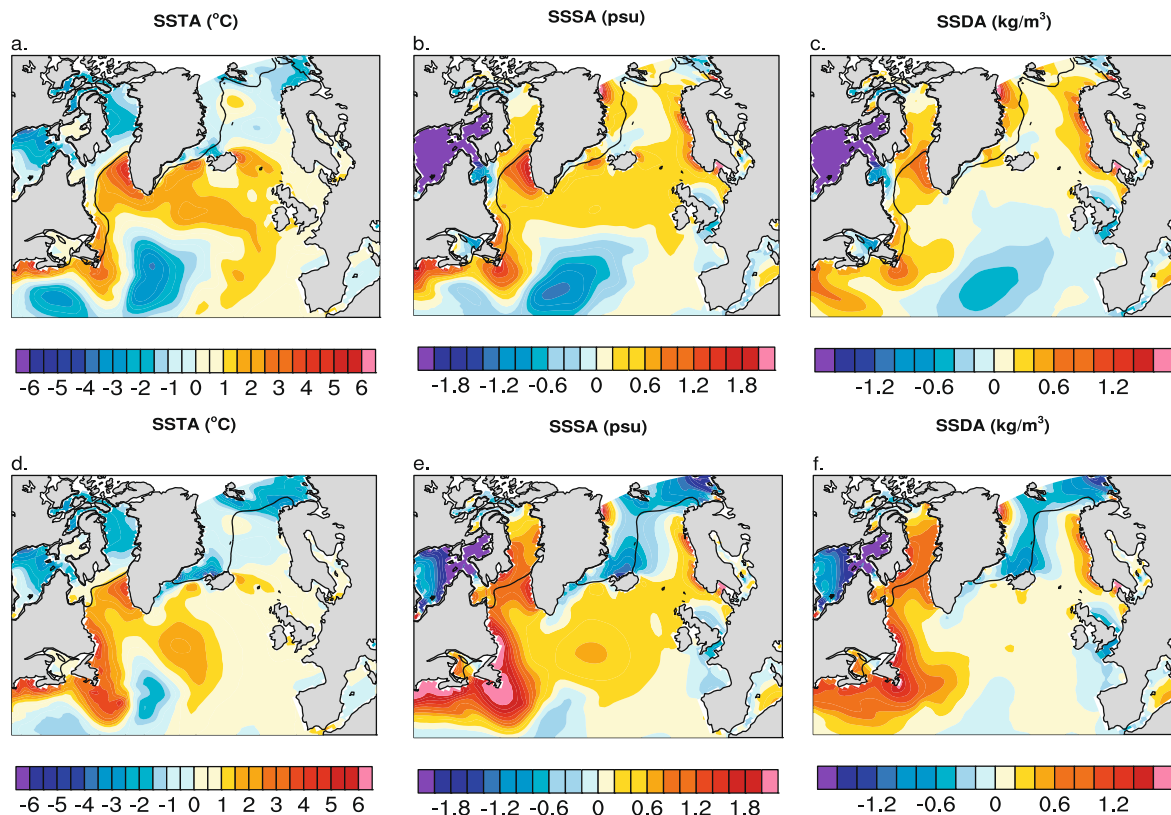


Fig. 6. Mean surface biases of temperature, salinity, and density from experiment A (a–c) and experiment B (d–f) from simulation years 54–58 (forcing years 2002–2006). The anomalies are computed relative to the WOA/PHC climatology. The black line indicates the 15% ice fraction contour from February of year 20.

In the first year, a strong NAC exists in both A and B near the observed longitude (42°W) which accounts for almost all of the northward transport of mass and heat across 48°N (Fig. 7, first row). The salt transport distributions (not shown) are similar to those for heat. A realistic Northwest Corner is evident in the barotropic flow field in the first year as a result of strong NAC transport north of 50°N . Southward transport is focused just west of the NAC, close to the Grand Banks shelf, and there is diffuse but significant southward transport east of 25°W . At year 5 (Fig. 7, second row), both experiments show a reduction in shelf transport and a drift of the core of the NAC to 30°W . This results in an increase in zonally-integrated northward heat transport across this latitude in both experiments. By year 20 (Fig. 7, third row), a distinct circulation pattern develops when the ice model is active. A branch of the NAC is maintained at 42°W in B but not in A. The NAC core in B stays west of the mid-Atlantic ridge at 30°W , but moves further east to 15°W in A. The net transport of heat across 48°N is comparable in the two experiments and remains so throughout the forcing cycle. Although the spun-up values of approximately 0.6 PW across 48°N are within the error range estimated from World Ocean Circulation Experiment (WOCE) hydrographic sections (Ganachaud and Wunsch, 2003), the longitudinal distribution of transport is realistic only in the first year of integration. A robust NAC along the shelf is simulated in year 58 of the hindcast (forcing year 2006) in B (Fig. 7, fourth row), and yet it is insufficient to reestablish the sharp property gradients and flow patterns which should exist in the Northwest Corner region (Fig. 3). Although the mid-Atlantic core of the NAC moves westward in this year, it remains incorrect. Eddy-resolving simulations suggest that barotropic meridional transports should be very small at this latitude east of 35°W (Frank Bryan, personal communication).

5. Time evolution

The spinup of the North Atlantic circulation in these experiments sheds light on the mechanisms linking the thermohaline circulation and GS path in a coarse resolution OGCM, and how they manifest under different surface boundary conditions. There is a sharp rise in the regionally-averaged Labrador Sea surface temperature (SST), surface salinity (SSS), and surface density (SSD) in the first few years of the case B hindcast (Fig. 8a–c). This rapid departure from observed climatology is mostly due to the effects of advection error. In contrast, positive and negative Labrador Sea surface biases in A largely cancel in the regional average early in the simulation, which is an artifact of spurious melt fluxes as described above. In both experiments, the penetration of overly warm, salty West Greenland Current water results in a rise in convective activity, evidenced by the increases in maximum mixed layer depth in the first decade of simulation (Fig. 8d). In B, the advent of deep mixing in the Labrador Sea to depths greater than 800 m is followed several years later by a rise in southward DWBC transport along the Grand Banks shelf at 43°N (Fig. 8e, where the transport is computed for density $\sigma_0 > 27.68$ kg/m^3 along the same zonal section shown in Fig. 4). By forcing year 1960, the total DWBC transport in B is close to the observed magnitude (17.5 Sv, S06) for this latitude. There is only a slight rise in DWBC transport in A to 5 Sv by forcing year 1965.

More than 80% of the DWBC transport in B is denser than $\sigma_0 = 27.8$ kg/m^3 (Fig. 9a), while A shows essentially zero southward shelf transport at such high density until much later in the simulation. The spinup of the dense DWBC in B reverses the weakening trend in the NAC transport (computed as the barotropic northward transport at 43°N between 50°W and 44°W) (Fig. 9b). A high correlation between the strengths of the DWBC and the

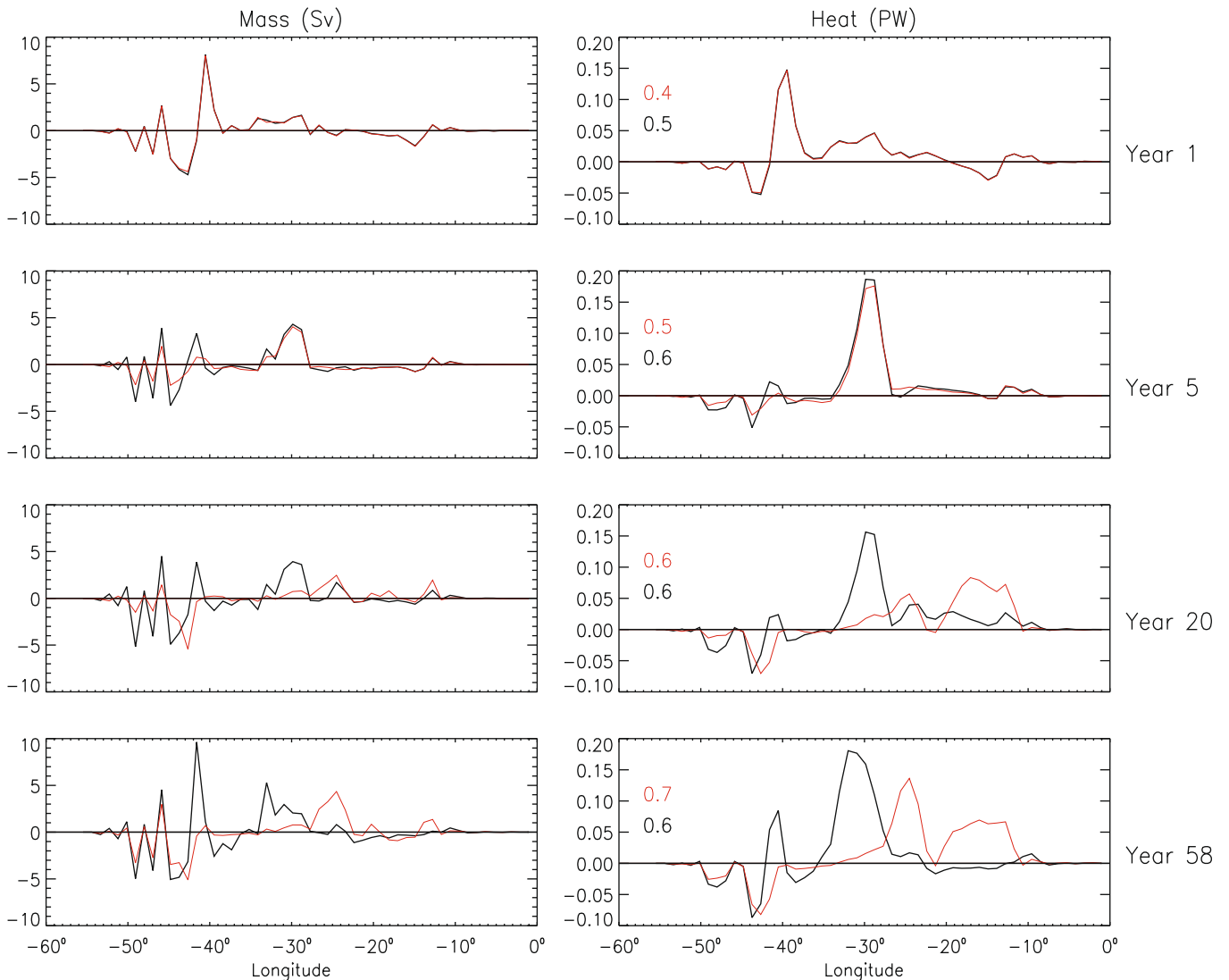


Fig. 7. Annual mean northward transport of mass (Sv) and heat (PW) across 48.3°N from case A (red) and B (black). The rows from top to bottom correspond to simulation year 1, 5, 20, and 58. The numbers indicate the zonally-summed heat transports across 48°N for the respective simulations. (For interpretation of the references to color in this figure legend, the reader is referred to the web version of this article.)

NAC is clearly evident in B. In all experiments, initialization with WOA/PHC induces a NAC offshore of the Grand Banks shelf of about 50 Sv, but this transport weakens to below 30 Sv throughout most of the simulation in A. Observations suggest a mean net northward volume transport across this section of near 140 Sv, with considerable seasonal and interannual variability (S04). Lower NAC transport leads to an increase in upper ocean temperature bias (increasingly negative) in a region east of the Grand Banks ($45\text{--}30^{\circ}\text{W}$, $43\text{--}52^{\circ}\text{N}$), and vice versa. This error growth is arrested in experiment B as a result of the rejuvenated shelf transports (Fig. 9c).

Correlations of the interannual variations in the metrics plotted in Figs. 8 and 9 are clearly discernible, and some “downstream” signals can be traced to variations in Labrador Sea surface conditions. For example, a forced surface freshening in the Labrador Sea in the late 1960s (Fig. 8b, the “Great Salinity Anomaly”; Dickson et al., 1988) inhibits deep convection in both A and B (Fig. 8d), with large subsequent drops in the early 1970s in DWBC transport (Fig. 8e), NAC transport (Fig. 9b), and NRG strength (Fig. 9d). The decrease in shelf transport is much larger in B, given the greater mean flow. Zhang and Vallis (2006) have discussed very similar

lagged adjustments of the North Atlantic circulation to realistically-varying salinity conditions in the Labrador Sea using a model which includes coupled atmospheric feedbacks. In their model, drops in DWBC transport in the early 1970s and mid to late 1980s are likewise accompanied by decreases in NRG strength, and northward shifts of the GS path which are in line with observations. The linear trend in the Atlantic MOC in A (Fig. 9e) is partly attributable to the steady increase in Labrador Sea SST and SSS and SSD, but hints of a trend are also evident in B. This Atlantic MOC trend is presumably a response to low frequency atmospheric variability, in particular the North Atlantic Oscillation, as has been argued by Eden and Willebrand (2001) and Biastoch et al. (2008).

To what degree are mixed boundary condition feedbacks contributing to the strength and variability of the thermohaline circulation? We address this question first by examining an ocean–ice coupled experiment configured equivalent to B except that a strong salinity restoring term was used to hold global SSS close to WOA/PHC values (experiment B1; $V_p = 50$ m/30 days). The blue curve in Fig. 8 shows that the strong restoring results in an average Labrador Sea surface salinity which stays very close to the observed regional average, with minimal interannual variability. As

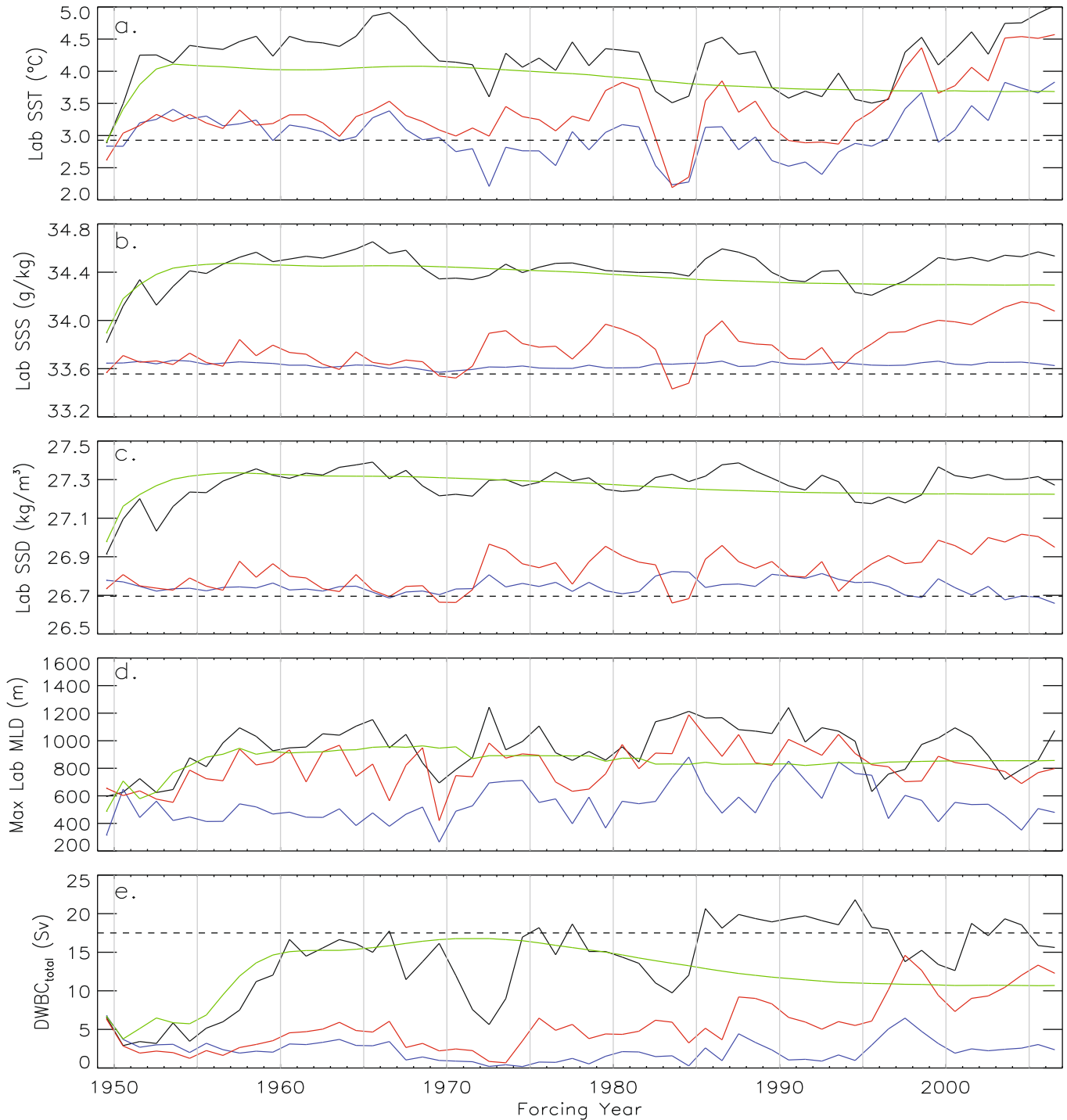


Fig. 8. Annual time series from experiments A (red), B (black), B2 (blue), and B3 (green) of regional-average Labrador Sea (a) sea surface temperature; (b) sea surface salinity; and (c) sea surface density (dashed lines indicate observed climatology from WOA/PHC); (d) annual maximum mixed layer depth in the Labrador Sea region; and (e) total DWBC transport across 43°N (computed as southward transport where $\sigma_0 > 27.68 \text{ kg/m}^3$ between 50°W and 46°W). (For interpretation of the references to color in this figure legend, the reader is referred to the web version of this article.)

a consequence, there is also a dramatic reduction in mean Labrador Sea SST compared to case B. The increase in deep convection and the spinup of the DWBC, NAC, and NRG seen in B are absent; the Labrador shelf ice edge is maintained (not shown); abyssal flow remains anemic throughout the Grand Banks shelf region (Fig. 5d); and the strength of the Atlantic MOC is reduced by about 35% (Fig. 9e). The B1 experiment strongly suggests that the overturning strength in experiments with weak salinity restoring (A and B) is spuriously robust. The rapid early increase in MOC strength in B

is replaced by a downward trend in the first decade, but the trend in MOC strength between 1965 and 2006 remains comparable to that seen in A and B, implying that this later signal is atmospherically-forced and not wholly attributable to boundary condition feedbacks. A disadvantage of using such a strong salinity restoring flux is readily apparent: damping the deviations of surface salinity from climatology defeats the purpose of using a model hindcast to study forced ocean variability, such as the “Great Salinity Anomaly” which has a minimal signature in the B1 simulation. The ther-

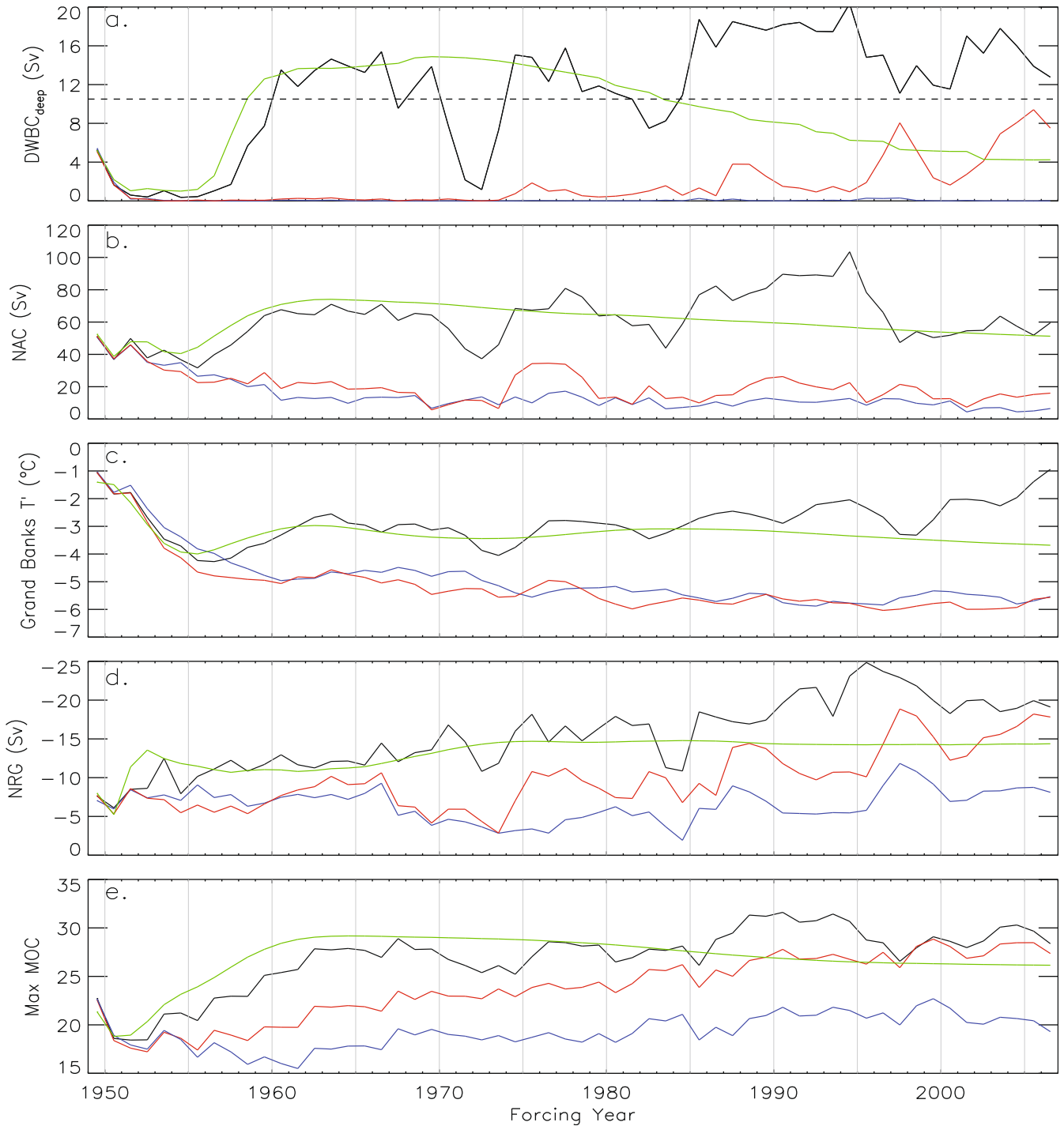


Fig. 9. Annual time series from experiments A (red), B (black), B2 (blue), and B3 (green) of (a) deep DWBC transport across 43°N (computed as southward transport where $\sigma_0 > 27.8 \text{ kg/m}^3$ between 50°W and 46°W), (b) NAC transport across 43°N (computed as northward barotropic transport between 50°W and 44°W), (c) regional-average temperature anomaly from WOA/PHC at 175 m in a box region east of Grand Banks (45°W–30°W, 43°N–52°N), (d) northern recirculation gyre strength (barotropic streamfunction minimum within the box region 70°W–45°W, 35°N–45°N), and (e) maximum Atlantic meridional overturning circulation (computed as the maximum in the Atlantic overturning streamfunction below 460 m and north of 28°N). (For interpretation of the references to color in this figure legend, the reader is referred to the web version of this article.)

mohaline circulation differences between A, B, and B1 show that the strength and variability of the Atlantic overturning is strongly dependent on boundary condition choices and the strength of the convection-transport feedback.

The interannually-varying atmospheric state, CORE2-IAF, maximizes the realism of the surface boundary condition in A and B to the extent possible, and adds significant forced variability to the

North Atlantic circulation. Experiment B1 demonstrates that the spinup of the high latitude bias and thermohaline circulations in A and B is strongly salinity-driven, but to what extent is this boundary condition feedback self-sustaining? When a repeating annual atmospheric state is used to force the coupled ocean-ice model (experiment B2), the transient thermohaline adjustment to Labrador Sea conditions becomes apparent. The green curve in

Fig. 8 shows that the rapid rise in Labrador Sea SSS, SST, and SSD occurs regardless of the atmospheric boundary conditions when the sea ice is prognostic, because inherent ocean model error drives the initial changes. The spinup of B2 is very comparable to B through simulation year 35, in terms of Labrador Sea surface conditions, meridional shelf transports, and gyre strength. After that, the DWBC and MOC in B2 weakens as Labrador Sea surface salinity trends lower. We conclude that the positive convection feedback accounts for most of the variability in the first decades of the B and B2 simulations, but it does not explain the steady increase in DWBC, NRG, and MOC strength seen later in the integration of B (Fig. 9a, d and e). A steady thermohaline circulation is achieved after roughly 50 years in B2 in which the high latitude salinity and density biases, the DWBC transport, and the gyre strength are maintained at levels below the early peak.

6. Water mass transformation

As implied above, the North Atlantic circulation in these coarse resolution OGCM experiments is highly sensitive to Labrador Sea water characteristics and the water mass transformation processes occurring in this region. The initial state of the Labrador Sea in each experiment is given by the WOA/PHC climatology, shown in T-S space in Fig. 10. The region is defined roughly as the area west of 46°W, north of 50°N, extending to Baffin Island's Cape Dyer in the north and excluding Hudson Strait (see Fig. 1). The region is further divided into four subregions: entering (along the west coast of Greenland to 65°N, where bathymetry < 3000 m); exiting (along the Labrador coast south of 57°N, where bathymetry > 3000 m); central Labrador Sea (east of 55°W, where bathymetry > 3000 m); and northern Labrador Sea water (remaining points). This climatology reflects the essential characteristics of the water mass transformation in this region which has been examined in detail using float measurements by Palter et al. (2008). These authors show that the distribution of T-S characteristics of the entering boundary current is centered around a temperature of 3.8 °C and a salinity value of 34.91. As a result of surface transformation and advective-diffusive mixing with central Labrador Sea water, the water which exits is fresher and cooler, centered around 3.4 °C and a salinity value of 34.86. The cluster of exiting water on the isopycnal $\sigma_0 = 27.74 \text{ kg/m}^3$ (Fig. 10) represents the Labrador Sea water which subsequently enters the DWBC. The least dense Labrador Sea water is also the freshest, and is found in the far north and along the Labrador Coast.

The feedback-driven northward heat and salt transport bias in A and B results in a steady drift in water mass properties in the Labrador Sea at all depths. After 50 years of integration, the water entering the Labrador Sea in case A is almost 2 °C warmer and 0.2 saltier, though not significantly denser, than observed (Fig. 10). The exiting water is likewise too warm and salty, and is characterized by an unrealistically tight T-S relationship which results from the specification of melt heat and freshwater fluxes under prescribed ice (see Appendix A). The change in density between entering water (blue) and exiting water (red) is somewhat larger than observed in A, so that by year 50 (historical year 1998) the anomalously dense exiting water generates a weak deep southward transport east of Grand Banks (Fig. 9a).

The stronger DWBC and more realistic NAC in coupled ocean-ice experiments (B, B2) are related to the significant volume of water exiting the Labrador Sea at density near $\sigma_0 = 27.8 \text{ kg/m}^3$ (Fig. 10). After 50 years of integration, the water entering the Labrador Sea in B is more than 1 °C too warm and 0.2 too saline. The density of entering water is biased positive since the anomalous T and S of the Greenland current is less density-compensating than in case A. The high density of exiting water in case B is primarily

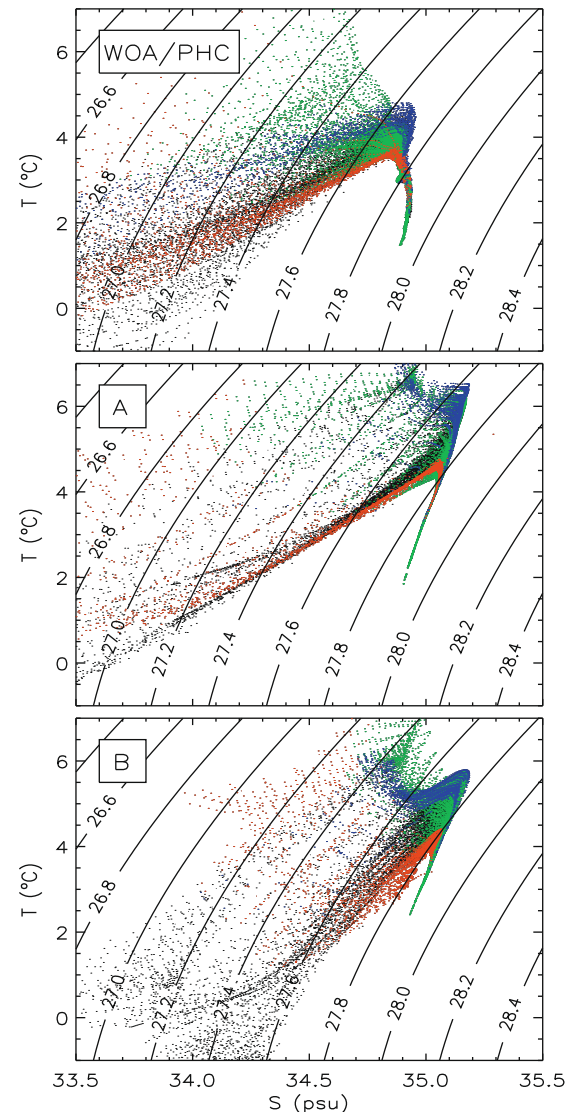


Fig. 10. Temperature-salinity diagram for Labrador Sea water from the WOA/PHC climatology (top) and from simulation year 50 (historical year 1998) of experiments A (middle) and B (bottom). The color scheme is as follows (see text for details): entering the Labrador Sea (blue); exiting the Labrador Sea (red); central Labrador Sea (green); northern Labrador Sea (black).

attributable to a spurious water mass transformation taking place within the Labrador Sea. Almost all of the water which advects into the region at density below $\sigma_0 = 27.7 \text{ kg/m}^3$ advects out at density greater than $\sigma_0 = 27.7 \text{ kg/m}^3$. The result is significant production of Labrador shelf water at $\sigma_0 = 27.8 \text{ kg/m}^3$, which is rarely seen in nature (Palter et al., 2008). The retreat of the Labrador coast ice edge contributes to the overly robust water mass transformation in experiment B and explains the prevalence of much denser and saltier water along the Labrador coast (red in Fig. 10) and in the northern region (black in Fig. 10).

6.1. Surface buoyancy fluxes

Because of transport feedbacks, the drift in Labrador Sea temperature and salinity is both a cause of, and an effect of, the reduced realism of the surface fluxes in this region. Positive SST biases in the Labrador Sea in both A and B generate excessive winter cooling (primarily latent and sensible) compared to air-sea flux estimates derived from the observed atmospheric state and corre-

sponding observed monthly SST (Large and Yeager, 2008, hereafter LY08). Early in the hindcast (simulation years 16–20), February heat loss in the Labrador Sea exceeds 400 W/m^2 in case A and 650 W/m^2 in case B, compared to the observed maximum heat loss of 250 W/m^2 during years 1964–1968.

The excessive cooling associated with the mixed thermohaline boundary conditions corresponds to excessive winter density flux (positive into the ocean) throughout the polar seas (Fig. 11). The surface density flux (D_0) is the sum of thermal and haline components computed from the net surface heat (H_0) and freshwater (F_0) fluxes as follows:

$$D_0 = D_{H_0} + D_{F_0} = -\frac{\alpha}{C_p} H_0 + \text{SSS} \frac{\rho}{\rho_0} \beta F_0 \quad (1)$$

where α and β are the coefficients of expansion for temperature and salinity; $\rho_0 = 1000 \text{ kg/m}^3$ is the density of freshwater; and C_p is the ocean heat capacity. In both experiments, the atmosphere is unrealistically efficient at extracting buoyancy from the surface ocean. An observed February density flux is computed from the LY08 interannual surface flux dataset paired with a sea surface density field computed from observed monthly SST which has been made compatible with observed sea-ice distributions (Hurrell et al., 2008) and WOA/PHC monthly climatological SSS. The LY08 field suggests that the winter air–sea flux of density into the ocean is maximum in the Irminger Sea near Iceland (Fig. 11). In the central Labrador Sea,

it reaches a monthly maximum of only $4 \text{ kg/m}^2/\text{s}$. The net Labrador Sea winter density flux is two times too large in A and more than three times too large in B.

The haline component of the density flux is likely to be small except near the ice edge, but ice–ocean flux fields are highly uncertain and were not included in the LY08 product due to a lack of data. In experiment A, the negative haline contribution associated with surface freshening when ice melts plays a significant role in counteracting the excess thermal density flux in the Labrador Sea (Fig. 11). This is certainly an exaggerated effect since the ice melt flux in this case does not reduce the sea ice extent. The ice melt flux and sea ice extent are more physically consistent with the ocean state in B which shows a minor haline contribution to the net density flux in the Labrador Sea. The larger ice-free region increases the positive net density flux bias since more warm water is exposed to cold air. The lack of ice (and ice melt) along the Labrador coast in B leads to a positive SSD bias throughout the Labrador Sea. In case A, ice melt flux in the Labrador Sea maintains SSD close to observed even though it is biased high in the eastern North Atlantic and Irminger Seas.

6.2. The role of surface water mass formation in setting DWBC strength

The excessive winter density flux (positive SST biases and reduced ice extent) in conjunction with overly dense surface condi-

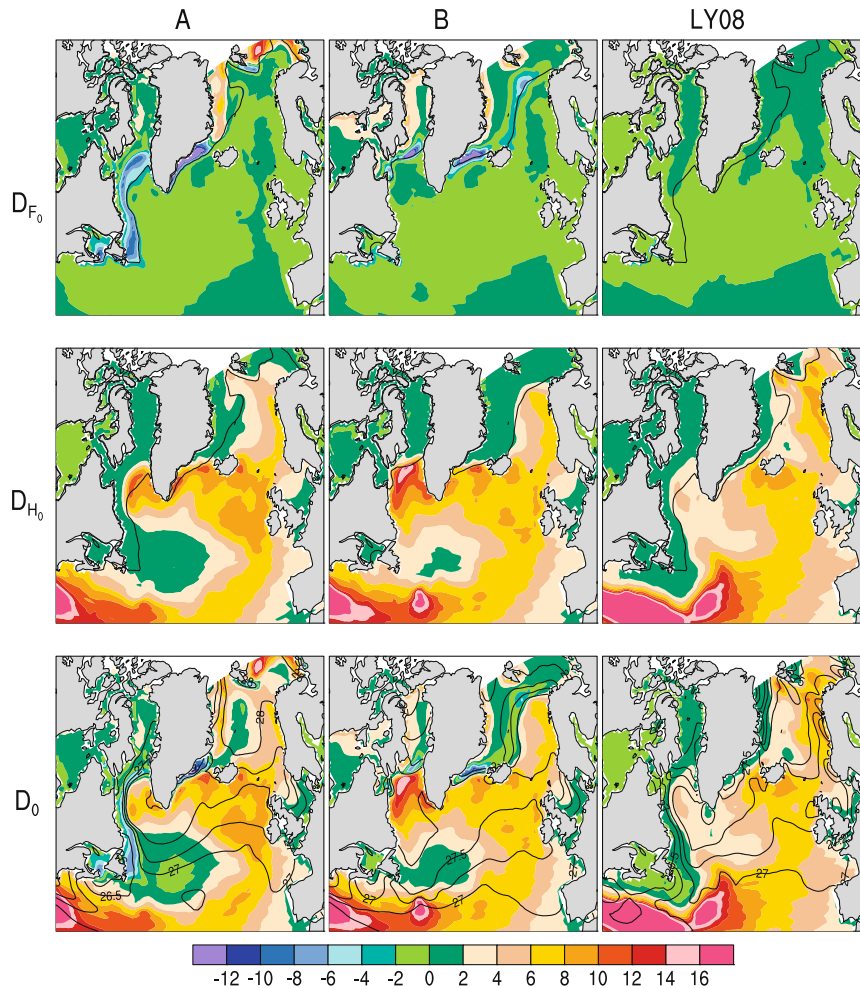


Fig. 11. Mean February surface density flux (averaged over simulation years 16–20, corresponding to historical years 1964–1968) from experiment A (left column), experiment B (middle column), and computed from the Large and Yeager (2008) monthly surface flux dataset (right column). The haline and thermal components of the density flux are shown in the top and middle rows, respectively, while the net density flux is shown in the bottom row. Density flux units are $\text{kg/m}^2/\text{s}$. The 5-year mean February 15% sea ice fraction contour is overlaid on the plots of D_{F_0} and D_{H_0} . Sea surface density contours (kg/m^3) are overlaid on the D_0 plot.

tions (positive SSS biases) leads to overproduction of overly dense water masses in these prescribed atmosphere experiments. Water mass formation driven by air–sea fluxes is determined from the surface density transformation rate, which is the surface integral of the density influx per unit of density (Speer and Tziperman, 1992; Large and Nurser, 2001):

$$F(\rho) = \frac{1}{\Delta\rho} \int_{\text{outcrop}} D_0 dA \quad (2)$$

The integral is performed over the region bounded by the surface outcrops of $\rho - \frac{\Delta\rho}{2}$ and $\rho + \frac{\Delta\rho}{2}$ with $\Delta\rho = 0.1 \text{ kg/m}^3$. The units of $F(\rho)$ are Sverdrups (Sv). The accumulation of water mass in the density range $d\rho$ resulting from surface transformation of density is then given by $-\frac{\partial F}{\partial \rho} d\rho$.

Regional water mass formation rates computed from monthly fluxes and averaged over years 16–20 of experiments A and B are compared in Fig. 12. In addition to the Labrador Sea region described above, which includes Baffin Bay in the following analysis, we consider a Greenland/Norwegian Sea region (roughly, north of 63°N and south of 75°N , see Fig. 1) and a North Atlantic region (north of 56°N , bounded to the west by the Labrador Sea and to the north by the Greenland/Norwegian Sea region). For compari-

son, the formation rates computed from the LY08 density flux dataset are plotted for the corresponding historical years (1964–1968). The isopycnals $\sigma_0 = 27.68 \text{ kg/m}^3$ and $\sigma_0 = 27.88 \text{ kg/m}^3$ demarcate the approximate density bounds of the observed DWBC east of Grand Banks (S06). A positive transformation rate indicates that the surface fluxes tend to increase the surface density, and vice versa; a negative slope indicates creation of a water mass at the given density while a positive slope indicates destruction of the water mass.

In each region, transformation rates in the simulations are large compared to LY08 and biased towards higher density classes, because the warm, salty surface bias increases both the SSD and the thermal density flux. Differences between the surface transformations in A and B help explain the differences in DWBC strength and density (Fig. 4, top panels) and gyre circulation (Fig. 2, top panels) seen during corresponding years. As in observations, the densest Atlantic waters are formed in the Greenland/Norwegian Seas in the model simulations, with comparable formation rate biases in A and B. There is somewhat greater formation of water with density greater than $\sigma_0 = 28.0 \text{ kg/m}^3$ in experiment A, since frazil ice formation in this region produces a positive haline transformation. This water mass (which in reality becomes Denmark Strait Over-

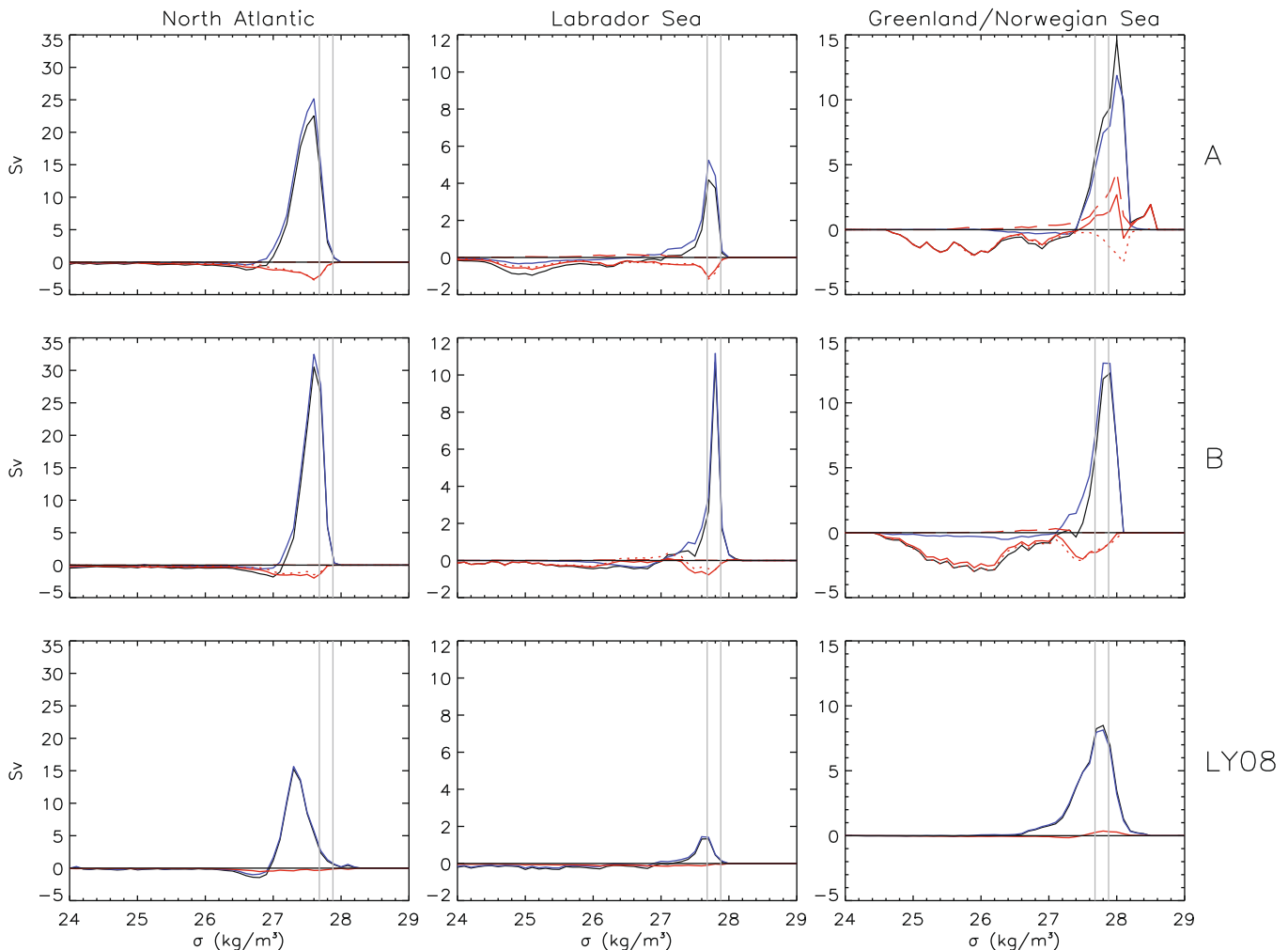


Fig. 12. Mean surface water mass transformation rates computed from years 16–20 (forcing years 1964–1968) of experiment A (top panels), B (middle panels), and the LY08 flux dataset (bottom panels) for three regions as a function of sea surface density. The components plotted are as follows: thermal (blue), haline (red), and total (black). The two dominant components of the haline transformation are also shown: melt flux (red, dotted) and frazil ice formation flux, F_f , (red, long dashed). The LY08 surface fluxes exclude ice melt and formation fluxes. The densities $\sigma_0 = 27.68 \text{ kg/m}^3$ and $\sigma_0 = 27.88 \text{ kg/m}^3$ are marked in grey to indicate the approximate density bounds of observed DWBC flow east of Grand Banks (S06). (For interpretation of the references to color in this figure legend, the reader is referred to the web version of this article.)

flow Water) may be too dense in the simulations to contribute to the model DWBC flow east of Grand Banks (Fig. 4). Observations (S06) suggest that there is at least 3.6 Sv of DWBC transport at density greater than $\sigma_0 = 27.88 \text{ kg/m}^3$. This might be better simulated with the inclusion of a parameterization for gravity current overflows, but such a parameterization is lacking in the experiments examined here.

Melt fluxes in the Greenland/Norwegian Seas form water in the range from $\sigma_0 = 25.5 \text{ kg/m}^3$ to $\sigma_0 = 26.0 \text{ kg/m}^3$ from denser water, but this transformation is again comparable in A and B and this density range is too low to contribute to the DWBC. The positive thermal density flux biases in the eastern North Atlantic and Irminger Sea region (Fig. 11) are of similar magnitude in both A and B, and consequently the North Atlantic transformation rates (Fig. 12, left panels) are only slightly different. The largest differences in surface water mass transformation rates are in the Labrador Sea (Fig. 12, center panels), where the maximum transformation rate is approximately 3 times too large in case A and 7 times too large in case B. High thermal density flux over a large area in B generates a peak transformation rate greater than 10 Sv at $\sigma_0 = 27.8 \text{ kg/m}^3$, which accounts for the strong DWBC transport in this density class in the prognostic sea ice experiment (Fig. 4). In A, there is much more negative transformation in the Labrador Sea, corresponding to ice-ocean (melt) flux, which produces lighter water and maintains a wide spread in the sea surface density. Consequently, the production of dense Labrador Sea water via air-sea exchange is confined to a much smaller geographic area in A (Fig. 11), and the peak transformation rate is much lower.

The haline component of the subpolar water mass transformation is much smaller than the thermal component when bulk flux forcing is used with either diagnostic or prognostic sea ice component. The negative density flux associated with sea ice melt is the dominant direct effect of the cryosphere on North Atlantic water mass properties. However, the indirect effect of the cryosphere on water mass production, namely the change in the area of direct air-sea interaction, is much more significant in the mixed boundary condition context, and this effect accounts for the large discrepancies in surface transformation (and DWBC transport and GS path) between experiments A and B.

6.3. The effect of salinity restoring boundary conditions

More realistic net transformation rates are seen when strong salinity restoring is used, as in experiment B1, but only through of the addition of very large and unphysical haline density fluxes. Since the restoring flux damps the mixed boundary condition transport feedback, thereby preserving the Labrador shelf ice edge in the ocean-ice coupled configuration, the thermal transformation rates are much lower in B1 compared to B. They are still high compared to LY08 since there is still some positive temperature bias at high latitudes. The salinity restoring flux is large and positive (tending to increase salinity and density) in the Greenland/Norwegian Sea region (not shown), where it counteracts larger melt fluxes in this region associated with increased northward heat transport in the far eastern Atlantic (the transports across 48°N in B1 resemble those from case A). In both the North Atlantic and Labrador Sea regions, a negative salinity restoring flux is the dominant term in the haline transformation, tending to maintain surface water of the appropriate climatological density despite advective salinity error and excess evaporation. Controlling salinity at these latitudes thus ensures surface water mass production at the correct density and near the correct rate. However, subsurface drift in high latitude water mass properties associated with circulation errors continues even in case B1, such that the Labrador Sea temperature and salinity distribution bears a strong resemblance to that in A after 50 years (Fig. 10).

7. Summary and discussion

With the help of an OGCM, we explore the connection between Labrador Sea, DWBC, and the Gulf Stream. Like many authors before, we find that increased buoyancy loss in the Labrador Sea leads to a strengthening of the DWBC. This then leads to a stronger northern recirculation gyre, and the subsequent reattachment of the Gulf Stream to the Grand Banks. The improved Gulf Stream path significantly reduces negative SST biases in the North Atlantic, which carries with it the hope that future climate simulations can provide a realistic Jet Stream and north European precipitation.

The ultimate source for the improved Gulf Stream path is the stronger buoyancy loss over the Labrador Sea. Because of the mixed boundary conditions, accurate buoyancy loss is strongly tied to an accurate path of the Gulf Stream and the NAC. Fig. 3 illustrates that, while case B clearly displays a better NAC position in the western North Atlantic, in all cases there is an eastward drift of the NAC core which results in spurious northward transport of warm and salty Gulf Stream water into the Irminger and Labrador Seas. The ultimate cause for these biases is not known, although it probably relates to the fact that the mechanism which maintains the strong near surface property gradients in the vicinity of the Northwest Corner is either absent or too weak in these simulations, even when the NAC offshore of Grand Banks is reasonably strong. This clearly warrants further investigation, because the eastward drift of northward transports results in the polar seas becoming too warm and salty, which is then exacerbated by a strengthening of the MOC.

If the Labrador Sea sea-ice concentration is restored to the observed values (case A), the implied melt water fluxes overcompensate for the salty bias, creating too light water and reducing convection. On the other hand, with a prognostic sea-ice model (case B), the salinity is not artificially changed, but now the warm water leads to a reduced sea-ice cover and excessive heat loss. This leads to an increase in deep ocean convection. These inconsistent responses are typical for any set of boundary conditions; however, in this particular location it leads to feedbacks which make the system sensitive to small errors in the salinity field.

In principle, this strong sensitivity could be realistic and one should really only be worried about the spurious NAC path in the east. However, a detailed comparison with observations shows that the new, much improved dynamics of the western boundary current regime is bought with water mass transformations far beyond the observed magnitude. Thus, there is a trade-off between dynamic and thermodynamic fidelity and apparently only one can be achieved. Strong restoring boundary conditions do not offer a satisfactory solution, since there is then neither dynamic nor thermodynamic fidelity, and although surface biases are reduced, the usefulness of the resulting simulation for studying oceanic variability is greatly diminished. In case B, physically consistent ocean-ice exchange and a more realistic DWBC/Gulf Stream flow is obtained with excessively large buoyancy losses in the Labrador Sea; in case A, spurious air-sea exchange is minimized and the diapycnal surface fluxes remain closer to observations, but the surface transformation degrades with time and the DWBC is too weak. The focus of future research should then be on two topics: Firstly, what causes the drift in the NAC path in the central to eastern basin? And secondly, why does it take excessively dense water to create a DWBC of realistic strength?

The first question is closely tied to the surface boundary conditions, because the subpolar gyre reaches to the ocean bottom and therefore is driven by buoyancy forcing and pressure torque as much as by the wind (Luyten et al., 1985). Thus, a slight bias in the NAC path may be amplified by the interaction with the bottom topography and mismatched boundary conditions. Semi-prognos-

tic methods which nudge the pressure field towards climatology in the Northwest Corner region lead to better NAC simulation in this class of model (Greatbatch et al., 2004; Weese and Bryan, 2006), suggesting that a better understanding of the mechanisms which sustain the pressure gradient would help direct the effort to simulate it correctly. We postulate that deficient initial conditions may also play a role in NAC detachment: since the ocean is initialized from rest, a geostrophic NAC is generated from the start, but the DWBC starts out very weak and quickly diminishes (Figs. 8 and 9), until a decade of simulation has elapsed in B. Given the dearth of deep velocity observations and the biases inherent in any coarse resolution OGCM velocity field, it is unclear how one could prescribe an adequate initial velocity field which might prevent the NAC drift in the first place.

The second question, or the question “what determines DWBC strength and position?”, is amply discussed in the literature. Apart from Labrador Sea buoyancy fluxes, it depends on abyssal upwelling (Stommel and Arons, 1960), strength of Arctic overflows (Warren, 1981), vertical eddy fluxes (Bryan et al., 2007), and shape of the bottom topography (ZV07). However, all of these are highly resolution dependent and not easily changed in a global OGCM. Increasing the abyssal upwelling and subsequent strengthening of the DWBC can be achieved by increased diapycnal diffusivity (Jochum, 2008), but its value is strongly constrained by global considerations (Menemenlis et al., 2005). The weakness of the modeled DWBC is probably partly related to insufficiently represented Arctic overflows, but the densest DWBC flow accounts for a relatively small fraction of the total (S06). Preliminary experiments with an overflow parameterization included in the most recent CCSM ocean model do not show significant enhancement of DWBC flow to the east and south of the Grand Banks (Gokhan Danabasoglu, personal communication). Vertical eddy fluxes as parameterized by Gent and McWilliams (1990) promise some control, but in practice the need to find a parameterization that provides a reasonable ACC transport puts a strong constraint on its structure (Eden et al., 2009). Thus, the present study, like many before it, suggests that while it is possible in principle to find physically-based controls for the OGCM representation of Gulf Stream and DWBC, in practice so many different sub-gridscale processes would have to be parameterized and tuned properly for the North Atlantic that the global fidelity of any OGCM is likely to suffer.

Finding a means to control DWBC strength is hindered by the fact that OGCMs with or without sea ice models suffer from the mismatch between observed atmospheric forcing and the modeled Gulf Stream position. Atmospheric models from coupled GCMs on the other hand, do not typically have the required resolution to create the strong storms with their large buoyancy loss which would seem to be necessary for realistic Labrador Sea water production. Thus, while the present study offers a glimmer of hope that the Gulf Stream path can be improved upon in climate models, it may well be that we will only be able to choose the nature of our biases. For example, for a climate study with less than 100 year duration, choosing the DWBC density biases over the Gulf Stream separation biases is an attractive choice because it will improve surface climate over the North Atlantic. For longer studies, however, it can be anticipated that the DWBC biases affect the density structure of the world ocean, and one will want to choose accurate NADW density over good Gulf Stream separation.

In this study, we demonstrate a link between Labrador Sea deep convection and Gulf Stream path in the non-eddy resolving ocean model component of the CCSM. As in the previous work of Zhang and Vallis (2006, 2007), we find that a strong, dense, downslope DWBC couples the thermohaline circulation to the gyre circulation in the North Atlantic via vortex stretching in the Grand Banks shelf region. The simulated DWBC is highly sensitive to high latitude surface boundary conditions, and in particular to salinity condi-

tions in the Labrador Sea, and is generally anemic unless temperature and salinity in the subpolar gyre deviate significantly from observed values. The magnitude of high latitude temperature and salinity biases in the North Atlantic, and consequently the strength of the DWBC and the NAC path, is shown to be strongly dependent on the choice of sea ice and salinity restoring boundary conditions. The primary conclusions of this study are as follows:

- High surface production of dense water in the Labrador Sea improves the North Atlantic circulation by generating a stronger, more realistic DWBC on the Grand Banks shelf which maintains a reasonable offshore NAC. As a result, general improvements are seen in the barotropic streamfunction and upper ocean temperature and salinity.
- Feedbacks associated with mixed surface boundary conditions result in unrealistically strong surface production of the densest North Atlantic water masses in CCSM 3.5 configurations of the 1° POP ocean model driven by a prescribed atmosphere. The feedbacks linking thermohaline forcing and gyre circulation are strengthened when a prognostic sea ice model is used, particularly when historical forcing is applied, and weakened when strong salinity restoring is used.
- There is a strong convolution of model error with diapycnal surface flux error in the North Atlantic which implies a low fidelity of hindcast thermohaline circulation variations in the Atlantic basin.

Acknowledgments

Helpful feedback from Peter Gent and two anonymous reviewers is gratefully acknowledged. We also thank Bill Large for the encouragement to pursue this research. This work was supported by the National Science Foundation through its sponsorship of the National Center for Atmospheric Research.

Appendix A. Data sea ice model

In the data ice model used for ocean only experiments, daily observed sea ice fraction obtained from the Special Sensor Microwave/Imager (SSM/I) (Comiso, 1999) defines $f_{SSM/I}$ at each model grid point. This areal coverage represents the only historical boundary condition in regions of sea ice, since under ice fluxes associated with sea ice melt (M), frazil ice formation (F), basal ice formation (B), and penetrating solar radiation (PS) are neither well constrained by observations nor amenable to specification through bulk formulae. Therefore, a crude heat budget is used to derive these fluxes in ocean only experiments. Following Large and Yeager (2004), the components of heat and freshwater exchange between the ice and ocean are:

$$Q_{io} = Q_M + Q_F + Q_B + Q_{PS} \quad (3)$$

$$F_{io} = F_M + F_F + F_B \quad (4)$$

When temperatures fall below freezing in the uppermost layer of the ocean model, temperature and salinity are adjusted by frazil ice formation fluxes which return the temperature to freezing within a timestep Δt , with an associated negative freshwater flux representing brine rejection:

$$Q_F = \rho_o C_p (\theta_f - \theta_1) \Delta_1 z \Delta t^{-1} \quad (5)$$

$$F_F = -Q_F A_f^{-1} \quad (6)$$

In the above, $\rho_o = 1026 \text{ kg/m}^3$ is the density of sea water, $C_p = 3996 \text{ J kg}^{-1} \text{ K}^{-1}$ is the heat capacity of sea water, $\theta_f = -1.8^\circ \text{C}$ is the freezing point of sea water, θ_1 is the temperature of the first

model layer, $\Delta_1 z = 10$ m is the thickness of the first model layer, and $A_f = 333,700 \text{ J kg}^{-1}$ is the latent heat of fusion. If the frazil ice forms where observed $f_{SSMI} = 0$, the frozen water content is accumulated locally and a fractional ice coverage is prescribed according to

$$W = -F_F \Delta t \quad (7)$$

$$f_{frazil} = \min(1.0, W/W_{max}) \quad (8)$$

where W_{max} ($= 1000 \text{ kg/m}^2$) is the water content threshold corresponding to complete grid cell coverage assuming an ice thickness of 1 meter. The air–sea fluxes of heat and freshwater derived from bulk formulae are applied only where $(1 - f_{ice})$ is non-zero, where

$$f_{ice} = f_{SSMI} + f_{frazil} \quad (9)$$

Momentum fluxes pass from air to sea regardless of ice coverage.

Whenever $Q_F > 0$, frazil ice is formed in the model and melt fluxes are set to zero ($Q_M = F_M = 0$). When $Q_F < 0$, the frazil ice formation terms are replaced by non-zero melt fluxes as long as surface ice exists ($f_{ice} > 0$). The amount of ice available for melting is considered infinite when $f_{SSMI} > 0$, but is limited by W when $f_{SSMI} = 0$. The negative heat and positive freshwater melt fluxes are thus

$$Q_M = \max(Q_F, Q_{min}), f_{SSMI} > 0 \quad (10)$$

$$Q_M = \max(Q_F, Q_{min}, -W A_f \Delta t^{-1}), f_{SSMI} = 0 \quad (11)$$

$$F_M = -Q_M A_f^{-1} \quad (12)$$

In the above, Q_{min} specifies a maximum melt rate generally set to -300 W/m^2 . If melt occurs where $f_{SSMI} = 0$, the accumulated frazil ice content (W) is reduced by $F_M \Delta t$. If frazil ice formation occurs where $f_{SSMI} > 0$, any accumulated frazil ice is eliminated ($W = 0$).

In the implementation of the data ice model used herein, the penetrating shortwave, Q_{PS} , and basal ice formation, Q_B , heat fluxes are set to zero, and the freshwater flux associated with basal ice formation, F_B , is prescribed from a monthly climatology obtained from a coarse resolution coupled ocean–ice simulation (Danabasoglu, 2004). This method was simple and deemed preferable to neglecting the basal terms altogether, but alternative treatments could be advocated given the large inherent uncertainties in specifying under-ice boundary conditions for uncoupled ocean models.

References

- Bjostoch, A., Boning, C., Getzlaff, J., Molines, J.-M., Madec, G., 2008. Causes of interannual-decadal variability in the meridional overturning circulation of the mid-latitude North Atlantic Ocean. *J. Climate* 21, 6599–6615.
- Brachet, S., Le Traon, P.Y., Le Provost, C., 2004. Mesoscale variability from a high-resolution model and from altimeter data in the North Atlantic Ocean. *J. Geophys. Res.* 109. doi:10.1029/2004JC002360.
- Bryan, F.O., Hecht, M.W., Smith, R.D., 2007. Resolution convergence and sensitivity studies with North Atlantic circulation models. Part I: the western boundary current system. *Ocean Modell.* 16, 141–159.
- Comiso, J., 1999. Bootstrap Sea Ice Concentrations for NIMBUS-7 SMMR and DMSP SSM/I. Digital Media, National Snow and Ice Data Center.
- Dai, A.G., Hu, A., Meehl, G.A., Washington, W.M., Strand, W.G., 2005. Atlantic thermohaline circulation in a coupled general circulation model: unforced variations versus forced changes. *J. Climate* 18, 2990–3013.
- Danabasoglu, G., 2004. A comparison of global ocean general circulation model solutions obtained with synchronous and accelerated integration methods. *Ocean Modell.* 7, 323–341.
- Danabasoglu, G., Large, W.G., Tribbia, J.J., Gent, P.R., Briegleb, B.P., 2006. Diurnal coupling in the Tropical oceans of CCSM3. *J. Climate* 19, 2347–2365.
- Danabasoglu, G., Marshall, J., 2007. Effects of vertical variations of thickness diffusivity in an ocean general circulation model. *Ocean Modell.* 18, 122–141.
- Danabasoglu, G., Ferrari, R., McWilliams, J.C., 2008. Sensitivity of an ocean general circulation model to a parameterization of near-surface eddy fluxes. *J. Climate* 21, 1192–1208.
- Dengg, J., Beckmann, A., Gerdes, R., 1996. The Gulf Stream separation problem. In: Krauss, W. (Ed.), *The Warmwatersphere of the North Atlantic Ocean*. Gebr. Borntraeger, pp. 253–290.
- Dickson, R.R., Meincke, J., Malmberg, S.-A., Lee, A.J., 1988. The great salinity anomaly in the northern North Atlantic 1968–1982. *Prog. Oceanogr.* 20, 103–151.
- Doney, S.C., Yeager, S.G., Danabasoglu, G., Large, W.G., McWilliams, J.C., 2003. Modeling Global Oceanic Inter-annual Variability (1958–1997): Simulation Design and Model-data Evaluation. Technical Report TN-452+STR, NCAR, pp. 48.
- Dukowicz, J.K., Smith, R.D., 1994. Implicit free-surface formulation of the Bryan–Cox–Semtner ocean model. *J. Geophys. Res.* 99, 7991–8014.
- Eden, C., Jochum, M., Danabasoglu, G., 2009. Effects of different closures for thickness diffusivity. *Ocean Modell.* 26, 47–59.
- Eden, C., Willebrand, J., 2001. Mechanism of interannual to decadal variability of the North Atlantic circulation. *J. Climate* 14, 2266–2280.
- Ezer, T., Mellor, G.L., 1992. A numerical study of the variability and separation of the Gulf Stream, induced by surface atmospheric forcing and lateral boundary flows. *J. Phys. Oceanogr.* 22, 660–682.
- Ferrari, R., McWilliams, J.C., Canuto, V.M., Dubovikov, M., 2008. Parameterization of eddy fluxes near oceanic boundaries. *J. Climate* 21, 2770–2789.
- Ganachaud, A., Wunsch, C., 2003. Large-scale ocean heat and freshwater transports during the world ocean circulation experiment. *J. Climate* 16, 696–705.
- Gent, P.R., McWilliams, J.C., 1990. Isopycnal mixing in ocean circulation models. *J. Phys. Oceanogr.* 20, 150–155.
- Gerdes, R., Koberle, C., 1995. On the influence of DSOW in a numerical model of the North Atlantic General Circulation. *J. Phys. Oceanogr.* 25, 2624–2642.
- Griffies, S.M., Biastoch, A., Boning, C., Bryan, F., Danabasoglu, G., Chassignet, E.P., England, M.H., Gerdes, R., Haak, H., Hallberg, R.W., Hazeleger, W., Jungclaus, J., Large, W.G., Madec, G., Pirani, A., Samuels, B.L., Scheinert, M., Gupta, A.S., Severijns, C.A., Simmons, H.L., Treguier, A.M., Winton, M., Yeager, S.G., Yin, J., 2009. Coordinated ocean–ice reference experiments (COREs). *Ocean Modell.* 26, 1–46.
- Greatbatch, R.J., Peterson, K.A., 1996. Interdecadal variability and oceanic thermohaline adjustment. *J. Geophys. Res.* 101, 20467–20482.
- Greatbatch, R.J., Sheng, J., Eden, C., Tang, L., Zhai, X., Zhao, J., 2004. The semi-prognostic method. *Cont. Shelf Res.* 24, 2149–2165.
- Hogg, N.G., Pickart, R.S., Hendry, R.M., Smethie Jr., W.M., 1986. The northern recirculation gyre of the Gulf Stream. *Deep-Sea Res.* 33, 1139–1165.
- Holland, M.M., Bitz, C.M., Hunke, E.C., Lipscomb, W.H., Schramm, J.L., 2006. Influence of the sea ice thickness distribution on polar climate in CCSM3. *J. Climate* 19, 2398–2414.
- Huffman, G., Adler, R., Arkin, P., Chang, A., Ferraro, R., Gruber, R., Janowiak, J., McNab, A., Rudolf, B., Schneider, U., 1997. The global precipitation climatology project (GPCP) combined precipitation data set. *Bull. Am. Meteor. Soc.* 78, 5–20.
- Hurlburt, H.E., Hogan, P.J., 2000. Impact of $1/8^\circ$ to $1/64^\circ$ on Gulf Stream model-data comparisons in basin-scale subtropical Atlantic Ocean models. *Dyn. Atmos. Oceans* 32, 283–330.
- Hurrell, J., Hack, J., Shea, D., Caron, J., Rosinski, J., 2008. A new sea surface temperature and sea ice boundary data set for the Community Atmosphere Model. *J. Climate* 19, 5145–5153.
- Jayne, S.R., 2009. The impact of abyssal mixing parameterizations in an ocean general circulation model. *J. Phys. Oceanogr.* 39, 1756–1775.
- Jochum, M., Danabasoglu, G., Holland, M., Kwon, Y.-O., Large, W.G., 2008. Ocean viscosity and climate. *J. Geophys. Res.* 113. doi:10.1029/2007JC004515.
- Jochum, M., 2008. The impact of latitudinal variations in vertical diffusivity on climate simulations. *J. Geophys. Res.* 114. doi:10.1029/2008JC005030.
- Joyce, T.M., Deser, C., Spall, M.A., 2000. The relation between decadal variability of subtropical mode water and North Atlantic oscillation. *J. Climate* 13, 2550–2569.
- Kalnay, E., Kanamitsu, M., Kistler, R., Collins, W., Deaven, D., Gandin, L., Iredell, M., Saha, S., White, G., Woollen, J., Zhu, Y., Chelliah, M., Ebisuzaki, W., Higgins, W., Janowiak, J., Mo, K., Ropelewski, C., Leetma, A., Reynolds, R., Jenne, R., 1996. The NCEP/NCAR 40-year reanalysis project. *Bull. Am. Meteor. Soc.* 77, 437–471.
- Large, W.G., Danabasoglu, G., Doney, S.C., McWilliams, J.C., 1997. Sensitivity to surface forcing and boundary layer mixing in a global ocean model: annual-mean climatology. *J. Phys. Oceanogr.* 27, 2418–2447.
- Large, W.G., Danabasoglu, G., McWilliams, J.C., Gent, P., Bryan, F.O., 2001. Equatorial circulation of a global ocean climate model with anisotropic horizontal viscosity. *J. Phys. Oceanogr.* 31, 518–536.
- Large, W.G., Nurser, G., 2001. Ocean Surface Water Mass Transformation. *Ocean Circulation and Climate*. Academic Press, pp. 317–336 (Chapter 5.1).
- Large, W.G., Yeager, S.G., 2004. Diurnal to Decadal Global Forcing for Ocean and Sea-ice Models: The Data Sets and Flux Climatologies. Technical Report TN-460+STR, NCAR, pp. 105.
- Large, W.G., Danabasoglu, G., 2006. Attribution and impacts of upper-ocean biases in CCSM3. *J. Climate* 19, 2325–2346.
- Large, W.G., Yeager, S.G., 2008. The global climatology of an interannually varying air–sea flux dataset. *Clim. Dyn.* doi:10.1007/s00382-008-0441-3.
- Levitus, S., Boyer, T., Conkright, M., Johnson, D., O'Brien, T., Antonov, J., Stephens, C., Gelfeld, R., 1998. Introduction, vol. 1. World Ocean Database 1998, NOAA Atlas NESDIS 18, pp. 346.
- Lohmann, G., Gerdes, R., Chen, D., 1996. Sensitivity of the thermohaline circulation in coupled oceanic GCM – atmospheric EBM experiments. *Clim. Dyn.* 12, 403–416.
- Luyten, J., Stommel, H., Wunsch, C., 1985. A diagnostic study of the northern Atlantic subpolar gyre. *J. Phys. Oceanogr.* 15, 1344–1348.
- Menemenlis, D., Fukumori, I., Lee, T., 2005. Using Green's functions to calibrate an ocean general circulation model. *Mon. Wea. Rev.* 133, 1224–1240.
- Oschlies, A., 2002. Improved representation of upper-ocean dynamics and mixed-layer depths in a model of the North Atlantic on switching from eddy-permitting to eddy resolving grid resolution. *J. Phys. Oceanogr.* 32, 2277–2298.

- Palter, J.B., Lozier, M.S., Lavender, K.L., 2008. How does Labrador Sea water enter the deep western boundary current? *J. Phys. Oceanogr.* 38, 968–983.
- Rahmstorf, S., Willebrand, J., 1995. The role of temperature feedback in stabilizing the thermohaline circulation. *J. Phys. Oceanogr.* 25, 787–805.
- Rosby, T., 1996. The North Atlantic Current and surrounding waters: at the crossroads. *Rev. Geophys.* 34, 463–481.
- Schmitz, W.J., McCartney, M.S., 1993. On the North Atlantic Circulation. *Rev. Geophys.* 31, 29–49.
- Schott, F.A., Zantopp, R., Stramma, L., Dengler, M., Fischer, J., Wibaux, M., 2004. Circulation and deep-water export at the western exit of the subpolar North Atlantic. *J. Phys. Oceanogr.* 34, 817–843.
- Schott, F.A., Fischer, J., Dengler, M., Zantopp, R., 2006. Variability of the deep western boundary current east of the Grand Banks. *Geophys. Res. Lett.* 33. doi:10.1029/2006GL026563.
- Smith, R.D., Dukowicz, J.K., Malone, R.C., 1992. Parallel ocean general circulation modeling. *Physica D* 60, 38–61.
- Smith, R.D., Maltrud, M.E., Bryan, F.O., Hecht, M.W., 2000. Numerical simulation of the North Atlantic Ocean at 1/10°. *J. Phys. Oceanogr.* 30, 1532–1561.
- Spall, M.A., 1996. Dynamics of the Gulf Stream/deep western boundary current crossover. Part I: entrainment and recirculation. *J. Phys. Oceanogr.* 26, 2152–2168.
- Speer, K., Tziperman, E., 1992. Rates of water mass formation in the North Atlantic Ocean. *J. Phys. Oceanogr.* 22, 93–104.
- Steele, M., Morley, R., Ermold, W., 2001. PHC: a global ocean hydrography with a high-quality Arctic Ocean. *J. Climate* 14, 2079–2087.
- Stommel, H., Arons, A.B., 1960. On the abyssal circulation of the world ocean. I. Stationary planetary flow patterns on a sphere. *Deep-Sea Res.* 6, 140–154.
- Tansley, C.E., Marshall, D.P., 2000. On the influence of bottom topography and the deep western boundary current on Gulf Stream separation. *J. Mar. Res.* 58, 297–325.
- Thompson, J.D., Schmitz, W.J., 1989. A limited area model of the Gulf Stream: design, initial experiments and model data intercomparison. *J. Phys. Oceanogr.* 19, 791–814.
- Treguier, A.M., Theetten, S., Chassignet, E.P., Penduff, T., Smith, R., Talley, L., Beismann, J.O., Boning, C., 2005. The North Atlantic subpolar gyre in four high-resolution models. *J. Phys. Oceanogr.* 35, 757–774.
- Warren, B.A., 1981. *Deep Circulation of the World Ocean. Evolution in Physical Oceanography.* MIT Press. pp. 6–41.
- Weaver, A.J., Sarachik, E.S., 1991. Evidence for decadal variability in an ocean circulation model: an advective mechanism. *Atmos. Ocean* 29, 197–231.
- Weese, S.R., Bryan, F.O., 2006. Climate impacts of systematic errors in the simulation of the path of the North Atlantic Current. *Geophys. Res. Lett.* 33. doi:10.1029/2006GL027669.
- Xie, P., Arkin, P.A., 1996. Analyses of global monthly precipitation using gauge observations, satellite estimates, and numerical model predictions. *J. Climate* 9, 840–858.
- Zhang, S., Greatbatch, R.J., Lin, C.A., 1993. A reexamination of the polar halocline catastrophe and its implications for couple ocean–atmosphere modeling. *J. Phys. Oceanogr.* 23, 287–299.
- Zhang, Y., Rossow, W., Lacis, A., Oinas, V., Mishchenko, M., 2004. Calculation of radiative flux profiles from the surface to top-of-atmosphere based on ISCCP and other global data sets: refinements of the radiative transfer model and input data. *J. Geophys. Res.* 109. doi:10.1029/2003JD004457.
- Zhang, R., Vallis, G.K., 2006. Impact of great salinity anomalies on the low-frequency variability of the North Atlantic Current. *J. Climate* 19, 470–482.
- Zhang, R., Vallis, G.K., 2007. The role of bottom vortex stretching on the path of the North Atlantic western boundary current and on the northern recirculation gyre. *J. Phys. Oceanogr.* 37, 2053–2080.